

Hydrodynamic Modeling for Stationary Breaking Waves

Final Report for Contract No. HR0011-04-C-0022

Prepared for:

The Defense Advanced Research Project Agency

By David T. Walker, Ales Alajbegovic and Jason D. Hunt

GENERAL DYNAMICS
Advanced Information Systems

"The views and conclusions contained in this document are those of the authors and should not be interpreted as representing the official policies, either expressly or implied, of the Defense Advanced Research Projects Agency or the U.S. Government."

DISTRIBUTION STATEMENT A
Approved for Public Release
Distribution Unlimited

August 2004

20041119 067

REPORT DOCUMENTATION PAGE**Form Approved**
OMB No. 0704-0188

Public reporting burden for this collection of information is estimated to average 1 hour per response, including the time for reviewing instructions, searching data sources, gathering and maintaining the data needed, and completing and reviewing the collection of information. Send comments regarding this burden estimate or any other aspect of this collection of information, including suggestions for reducing this burden to Washington Headquarters Service, Directorate for Information Operations and Reports, 1215 Jefferson Davis Highway, Suite 1204, Arlington, VA 22202-4302, and to the Office of Management and Budget, Paperwork Reduction Project (0704-0188) Washington, DC 20503.

PLEASE DO NOT RETURN YOUR FORM TO THE ABOVE ADDRESS.**1. REPORT DATE (DD-MM-YYYY)**

08-08-2004

2. REPORT TYPE

Final

3. DATES COVERED (From - To)

09 Nov 2003 - 08 Aug 2004

4. TITLE AND SUBTITLE

Hydrodynamic Modeling for Stationary Breaking Waves

5a. CONTRACT NUMBER

HR0011-04-C-022

5b. GRANT NUMBER**5c. PROGRAM ELEMENT NUMBER****6. AUTHOR(S)**

Walker, David T., Alajbegovic, Ales, and Hunt, Jason D.

5d. PROJECT NUMBER**5e. TASK NUMBER**

1

5f. WORK UNIT NUMBER**7. PERFORMING ORGANIZATION NAME(S) AND ADDRESS(ES)**General Dynamics Advanced Information Systems
PO Box 134008
Ann Arbor, MI 4811304008**8. PERFORMING ORGANIZATION
REPORT NUMBER**

200392-8-F

9. SPONSORING/MONITORING AGENCY NAME(S) AND ADDRESS(ES)Defense Advanced Research Projects Agency
3701 North Fairfax Drive
Arlington, VA 22203**10. SPONSOR/MONITOR'S ACRONYM(S)**

DARPA

**11. SPONSORING/MONITORING
AGENCY REPORT NUMBER****12. DISTRIBUTION AVAILABILITY STATEMENT**

Approved for Public Release: Distribution Unlimited

13. SUPPLEMENTARY NOTES**14. ABSTRACT**

In this study, approaches for calculating the hydrodynamics of breaking waves were examined and the impact of hydrodynamic model errors on the prediction of radar backscatter was assessed. Reynolds-averaged Navier-Stokes (RANS) computations of stationary hydrofoil-generated breaking waves were carried out, including the modeling of the breaking region. These results were compared to experimental data. A subset of these results was used as input to the Veridian scattering model (VSM) and the results were also compared to available data. The results were then used define the research needs in this area.

15. SUBJECT TERMS

Breaking waves, Reynolds-averaged modeling, Potential flow

16. SECURITY CLASSIFICATION OF:**a. REPORT**
U**b. ABSTRACT**
U**c. THIS PAGE**
U**17. LIMITATION OF
ABSTRACT**
SAR**18. NUMBER
OF PAGES**
48**19a. NAME OF RESPONSIBLE PERSON**
David T. Walker**19b. TELEPHONE NUMBER (Include area code)**
(734)994-1200 x2987

Contents

Contents	i
List of Figures.....	ii
Summary	1
Introduction	3
Approach	5
<i>RANS Computations</i>	5
<i>Potential Flow Computations</i>	6
<i>Breaking Model</i>	7
<i>Short-Wave Modeling</i>	8
<i>Radar Backscatter Model</i>	9
RANS Implementation	10
<i>Wave Reflections from Domain Boundaries</i>	10
<i>Computational Domain</i>	10
<i>Grid Variations</i>	11
Results	14
<i>Non-Breaking Waves</i>	14
<i>Breaking Waves</i>	17
<i>Radar Backscatter Modeling</i>	23
Conclusions and Recommendations	29
<i>Conclusions</i>	29
<i>Research Needs</i>	30
References	33
Appendix: Nonlinear Free-Surface Potential-Flow Computation Involving a Hydrofoil.....	35

List of Figures

Figure 1. Flow geometry showing a) pressure and b) velocity fields; c) and d) the morphology of the breaking wave (Furey <i>et al.</i> , 2003).....	6
Figure 2. Schematic of the breaker and the definitions of the modeling parameters.....	7
Figure 3. Mesh used in the simulation: a) mesh extension before the hydrofoil, b) mesh detail around the hydrofoil, c) mesh extension after the hydrofoil.	11
Figure 4. The calculated wave profile for the Duncan 0.261 m case shown for the entire computational domain.	11
Figure 5. Meshes used in the simulations: a) Cartesian mesh and b) C-mesh.	12
Figure 6. Results calculated on the Cartesian and C-meshes for the Duncan 0.210 m case obtained with UNCLE. Shown are a) wave profiles and b) surface pressure distributions.	13
Figure 7. Results calculated with CFDSHIP-IOWA and UNCLE for the Duncan 0.261 m case. Shown are a) wave profiles and b) surface pressure distributions.....	13
Figure 8. Computational results for the flow over the submerged hydrofoil moving with speed 0.8 m/s, depth of submergence 0.261m and angle of attack 5° (Duncan, 1983): a) dynamic pressure field, b) axial velocity field, and c) turbulence kinetic energy field.....	15
Figure 9. Computational results obtained with CFDSHIP-IOWA and the potential flow code for the Duncan 0.261 m case.....	16
Figure 10. Comparison between the results obtained with CFDSHIP-IOWA and the potential flow code for the first case by Furey <i>et al.</i> (2003) – CWC Case 1.	17
Figure 11. Comparison between the predicted and measured wave profiles for the cases measured by Duncan (1983). Plots on the left side were obtained without the breaking wave model, while plots on the right were obtained with the breaking wave model turned on.....	18
Figure 12. Computational results for the flow over the submerged hydrofoil moving with speed 0.8 m/s, depth of submergence 0.185 m and angle of attack 5° (Duncan, 1983): a) dynamic pressure field, b) axial velocity field, and c) turbulence kinetic energy field.....	19
Figure 13. Comparison between the predicted and measured wave profiles for the cases measured by Walker <i>et al.</i> (1996). Simulations were performed at different breaker heights, h^* , used in the breaking wave model.....	20
Figure 14. Comparison between the predicted and measured wave profiles for the data by Furey <i>et al.</i> (2003). Simulations were performed at inlet velocities measured by the Pitot tube (left column) and by the Acoustic Doppler Velocimeter (right column).	22
Figure 15. Radar cross-section results for the small-perturbation method (SPM) calculated using the experimentally measured short-wave spectrum, compared to experimental observations for both HH and VV polarization (from Ericson <i>et al.</i> 1999): a) 3 degree angle of attack, down-	

wave look direction; b) 3 degree angle of attack, up-wave look direction; c) 4 degree angle of attack, down-wave look direction; d) 4 degree angle of attack, up-wave look direction.23

Figure 16. Hydrodynamic and SPM radar backscatter predictions for 3 degree case of Walker et al. (1996): a) mean surface elevation; b) RMS surface elevation; c) radar cross section for HH polarization, up-wave look direction; d) HH, down-wave; e) VV, up-wave; f) VV, down-wave.....25

Figure 17. Comparison of measured (upper) and predicted (lower) streamwise velocity components at surface for the 3 degree angle of attack wave from Ericson et al. (1999). Experimental data from Ericson et al., computations using CFDSHIP-IOWA. The dashed red line indicates the location of breaking in the RANS predictions.....26

Figure 18. Hydrodynamic and SPM radar backscatter predictions for 4 degree case of Walker et al. (1996): a) mean surface elevation; b) RMS surface elevation; c) radar cross section for HH polarization, up-wave look direction; d) HH, down-wave; e) VV, up-wave; f) VV, down-wave.....27

Summary

This study had two goals, the first of which was to examine approaches for calculating the hydrodynamics of breaking waves and to assess the impact of hydrodynamic model errors on the prediction of radar backscatter. To address this, Reynolds-averaged Navier–Stokes (RANS) computations of stationary hydrofoil-generated breaking waves were carried out, including the modeling of the breaking region. These results were compared to experimental data. To determine the impact of the errors in hydrodynamic modeling on predictions of radar backscatter, a subset of the hydrodynamic results were used as input to the Veridian Scattering Model (VSM) and the results were compared to those of Ericson et al. (1999) which uses similar backscatter modeling but with experimentally measured hydrodynamic inputs. The second goal of this study was to use the information gained through this effort to define the research needs in this area.

The conclusions of the study are that computations of breaking waves produce qualitatively correct behavior, in the sense that energy is dissipated, turbulence is produced in the breaking region and the wave amplitude is reduced; however, the results are not particularly accurate and the present methods are not robust. For some cases the wave amplitude was over-estimated and for some it was under-estimated, indicating incorrect amounts of dissipation from the breaking model, while for some cases, a converged solution could not be obtained at all. For a subset of the cases, the VSM radar backscatter model was used to estimate both the RMS surface fluctuation level and the radar cross-section (RCS) for X-Band at 45 degrees incidence. The RMS surface fluctuations in all cases drop too slowly as the short waves propagate downstream from the breaking region. This is traced to the fact that the RANS-predicted velocity field in the breaking region is not accurate. The radar cross-section was estimated using the small-perturbation method (SPM) and the results were compared to those generated using the SPM model with the correct hydrodynamic inputs, derived from experimental observations, presented in Ericson et al. (1999). Overall, the peak RCS values for the breaking region tend to be over-estimated by as much as 12 dB, and the downstream RCS values tend to be over-estimated by as much as 25 dB when compared to the results of the SPM model using the correct hydrodynamic inputs. Hence, hydrodynamic errors incurred in modeling breaking waves can lead to significant errors in radar backscatter estimates.

A number of areas where research is needed have been identified. In order to predict the behavior of breaking waves for flows of practical interest, approaches such as the Reynolds-averaged Navier–Stokes equations must be employed. This type of approach requires that some of the details of the flow must be represented by models which need to accurately reflect the important physical processes. The results of this study indicate that improvements must be made in virtually all aspects of modeling wave breaking. These include modeling the onset of wave breaking, modeling the generation of surface disturbances in the breaking region, predicting the propagation of short waves through and beyond the breaking region, and development of proper free-surface boundary conditions. Another important research area is development of more robust and efficient computational approaches, including radiation boundary conditions and efficient solvers.

To undertake the development of improved modeling approaches, new, more detailed information on the behavior of breaking waves is required. There are two complementary ways in which this information can be obtained: The first is through direct numerical simulations (DNS) based on numerical solution of the exact governing equations for the three-dimensional time-evolution of breaking waves. DNS allows the details of the waves to be examined both qualitatively and quantitatively, and can provide access to un-measurable quantities such as the subsurface pressure fluctuations. These detailed data can be used to guide the development of the needed models. The drawback to this approach is that presently it can only be applied to relatively short breaking waves (i.e. waves substantially less than a meter in wavelength) and even then it taxes available computing resources. The second approach for obtaining the needed

information is experimental studies of breaking waves. Here, a more limited set of information can be obtained using available measurement technology, but this can be done for the range of scales from DNS to scales approaching situations of practical interest. Detailed measurement of surface structure, velocity and subsurface turbulence are needed. Through a coordinated, combined approach of DNS and experiments, the information necessary to develop first-principles models for wave breaking and the associated small-scale disturbances important for radar backscatter can be obtained.

A final issue is the framework within which modeling of breaking waves should be addressed. Reynolds-averaged approaches do not exclude any of the physical processes which naturally occur in wave breaking, hence RANS approaches should be able to predict wave breaking accurately, given appropriate models. For robustness, it appears that a computational approach which admits overturning waves (multiple-valued free surface), such as a level-set or an improved surface-tracking approach, will be needed. Potential flow methods impose some requirements on the flow (inviscid, irrotational) which are violated in breaking waves; however, potential flow methods are significantly less demanding computationally. For this reason, potential flow methods would be attractive, if they could be extended to model wave breaking without resorting to ad-hoc approaches. This should be investigated as well.

Introduction

Breaking waves on the ocean surface can yield a significant radar return; however, the prediction of radar backscatter from breaking waves is limited by our ability to predict the details of the mean velocity field and surface shape as well as the small-scale hydrodynamic disturbances which result from wave breaking. The first goal of this study was to examine approaches for calculating the hydrodynamics of breaking waves and to assess the impact of hydrodynamic model errors on the prediction of radar backscatter. To address this, first the hydrodynamic models were used to calculate the mean surface elevation and velocity fields for two-dimensional stationary hydrofoil-generated waves. These results were compared to available experimental data. To determine the impact of the errors in hydrodynamic modeling on predictions of radar backscatter, a subset of the hydrodynamic results were used as input to the Veridian Scattering Model (VSM). The VSM radar-cross-section results could then be compared to data to assess the end-to-end performance of the combined hydrodynamic–radar-backscatter modeling approach.

The second goal of this study was to use the information gained through this effort to define the research needs in this area. To calculate radar backscatter, the two-dimensional energy spectrum of the small-scale waves is needed, along with the mean surface slope. The ability to calculate these quantities will be assessed, and the deficiencies in the approaches will be identified. This will identify areas where new approaches or new knowledge are required.

Hydrodynamic predictions of waves can be made via numerical solution of the Navier–Stokes equations subject to the appropriate free-surface boundary conditions. For practical flows which are steady in the mean, simplifications to these equations must be made in order to make the computations feasible. Two approaches for this exist: potential flow, where viscous and rotational effects are formally eliminated from the equations, and Reynolds-averaged approaches, where the equations are time-averaged. Potential flow calculations are significantly faster, but cannot account for viscous effects or turbulence. Reynolds-averaged Navier–Stokes (RANS) calculations require significantly more computational effort, as well as turbulence modeling, but are a framework which can accommodate both viscous and turbulence effects.

In typical calculations of waves with either RANS or potential flow, wave breaking is not considered and solutions can be obtained, even for very steep waves which in the real world would break. In this case, the surface elevation and velocity fields predicted are solutions to the equations, but are incorrect, and radar backscatter predictions based on these results will also be incorrect. If the waves become steep enough, either RANS or potential flow computations will fail unless a breaking model is invoked. Modeling the effects of wave breaking is presently relatively crude, relying on corrections to the surface pressure and velocity that stabilize the steep wave and prevent overturning.

The small-scale unsteady surface disturbances generated by wave breaking are important for radar backscatter; however, modeling the generation of short waves by wave breaking has not been addressed in a significant way by the hydrodynamics community. An empirical model for the short-wave spectrum in the breaking region of a stationary wave has been developed (see e.g. Walker et al. 1996). This empirical spectrum is used in VSM (Ericson & Wackerman 2000) to prescribe the behavior of the short waves in the breaking region. The propagation of short waves as they leave the breaking region and interact with the surrounding surface velocity field is calculated via solution of the wave-action balance equations (Komen et al. 1994), which then provides the short-wave spectrum for the entire surface. To accomplish this, VSM requires a description of the large-scale mean hydrodynamics (surface elevation, surface velocity) along with a map of the breaking regions. These inputs are derived from either RANS or potential-flow solutions. An alternative approach is to specify a turbulence-related short-wave source term directly in the action balance equations (Walker 2000). This has not been applied to breaking waves, but has been used in other flows.

Given the short-wave spectrum, the radar backscatter can be estimated using different approximate theories. The comparisons to be made in this study will be for laboratory measurements at moderate incidence angles ($\pm 45^\circ$). For this case the small-perturbation method (SPM), as described by Ericson et al (1999) is used.

In the following sections, first the hydrodynamic modeling is described and issues of model type and grid resolution are addressed. Then hydrodynamic results calculated for breaking waves are shown and compared to available experimental data. The hydrodynamic results are then used as a basis for radar backscatter predictions and again compared to experimental data.

Approach

Hydrodynamic model calculations were carried out mainly using a Reynolds-averaged Navier–Stokes (RANS) approach; however, as a check on the accuracy of those solutions, potential flow calculations were performed as well for some cases. Results from two different RANS codes, CFDSHIP-IOWA and UNCLE, which have different numerical formulations, were used, so as to rule out systematic errors. The RANS solutions for some of the cases examined diverged, because the predicted waves became too steep and overturned. To deal with these cases, a wave-breaking model, which redistributes momentum and dissipates energy in the waves was used. Finally the RANS results for a subset of the cases were used as input to radar backscatter computations using VSM. The approaches used for each of these are described here.

RANS Computations

Reynolds Averaged Navier-Stokes (RANS) governing equations are:

$$\nabla \cdot \mathbf{u} = 0 \quad (1)$$

$$\rho \left(\frac{\partial \mathbf{u}}{\partial t} + \mathbf{u} \cdot \nabla \mathbf{u} \right) = -\nabla p + \mu \nabla^2 \mathbf{u} - \nabla \cdot \boldsymbol{\tau}_t + \rho \mathbf{g} \quad (2)$$

where $\boldsymbol{\tau}_t$ is the Reynolds stress. The Reynolds stress is calculated either using the k - ϵ model from the Boussinesq hypothesis or directly from a Reynolds-stress model (RSM). Boundary conditions imposed on the free surface is the kinematic boundary condition

$$\frac{\partial \eta}{\partial t} + \mathbf{u} \cdot \nabla \eta = w \quad \text{on } z = \eta(x, y, t), \quad (3)$$

and the dynamic boundary condition

$$-p\mathbf{n} + \mu(\nabla \mathbf{u} + \nabla \mathbf{u}^T) \cdot \mathbf{n} = -p_{ATM} \mathbf{n}. \quad (4)$$

The solution of the RANS equations is obtained using two Computational Fluid Dynamics (CFD) codes: CFDSHIP-IOWA and UNCLE.

CFDSHIP-IOWA is based on the Finite Difference Method (FDM) that solves the equations in three-dimensional space and unsteady mode (Paterson *et al.*, 2003). It includes a free surface tracking capability, where the computational grid is fitted to the free-surface boundary. Turbulence is modeled with a two-equation k - ϵ model. The code is being used primarily for the study of ship hydrodynamics and is considered a state-of-the-art code for this type of problems. The code is parallelized and can be run using Message Passing Interface (MPI).

UNCLE is based on the Finite Volume Method (FVM). The equations are solved in three-dimensions and the simulations can be performed both in steady and unsteady modes. The convection terms are discretized using the Roe's flux-splitting approach, and the momentum equations are solved in a coupled manner. Turbulence is modeled either with the k - ϵ or full Reynolds Stress Model (RSM). The calculation of the turbulence model is decoupled from the calculation of the velocity components. It also has the surface tracking capability and can be run in parallel mode using MPI.

Potential Flow Computations

In case of incompressible, inviscid, irrotational flow, it is possible to define a potential, Φ , so that the velocity is given by the gradient of a scalar potential function,

$$\mathbf{u} = \nabla \Phi. \quad (5)$$

Using such a definition of the potential, the governing equations can be rewritten as:

$$\nabla^2 \Phi = 0 \quad (6)$$

$$\frac{\partial \Phi}{\partial t} + p + \frac{1}{2} \rho \nabla \Phi \cdot \nabla \Phi + \rho g z = C(t) \quad (7)$$

Consequently, the kinematic and dynamics boundary conditions become equal to:

$$\frac{\partial \eta}{\partial t} + \nabla \Phi \cdot \nabla \eta = \Phi_z \quad \text{on } z = \eta(x, y, t) \quad (8)$$

$$p = 0 \quad (9)$$

The potential flow equations are solved using a de-singularized potential method (Scullen & Tuck, 1995; Scullen, 1998). The effects of the submerged hydrofoil are implemented with a linearly varying vortex panel method (Kuethe & Chow, 1986). This implementation is described in detail in the Appendix, below.

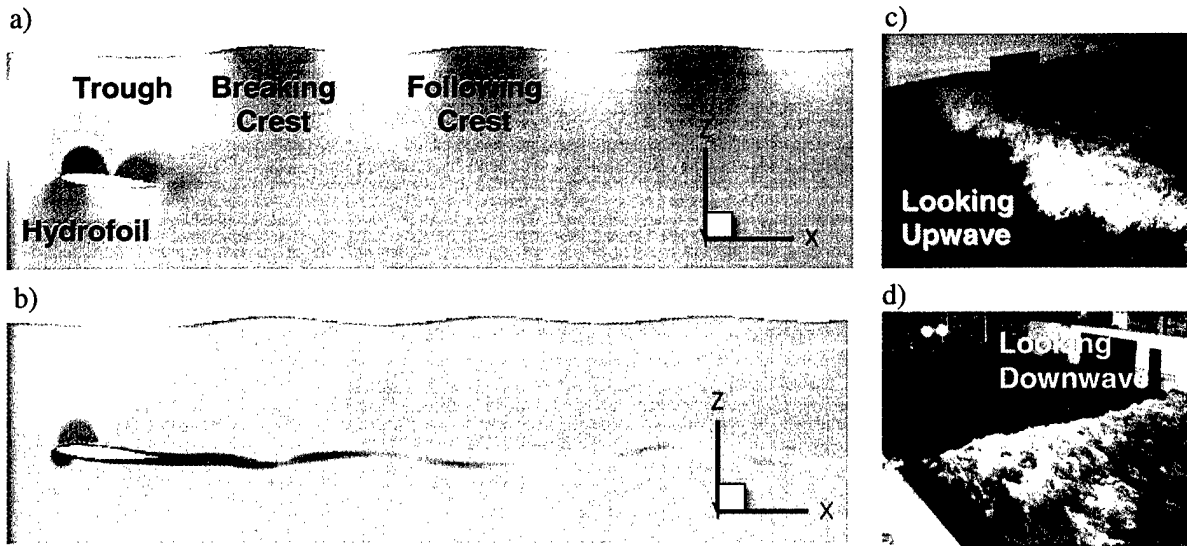


Figure 1. Flow geometry showing a) pressure and b) velocity fields; c) and d) the morphology of the breaking wave (Furey *et al.*, 2003).

Breaking Model

For hydrofoil-generated waves, a trough forms above the hydrofoil, followed by a wave train. If the disturbance caused by the foil is large enough, due either to the depth of the foil or its angle of attack, the initial wave crest will break. Typical pressure and velocity fields in such a case are shown in Figure 1a) and Figure 1b). Theory indicates that the orbital velocities associated with the waves increase in proportion to the wave amplitude. When the orbital velocity at the wave crest exceeds the phase velocity of the waves, the waves will break. The process can be very abrupt as in the case of a plunging breaker, or more tempered as a spilling breaker (Figure 1c and Figure 1d). The spilling breaker causes both velocity and pressure modification close to the wave surface. Simulation of the wave under breaking conditions requires the inclusion of these effects.

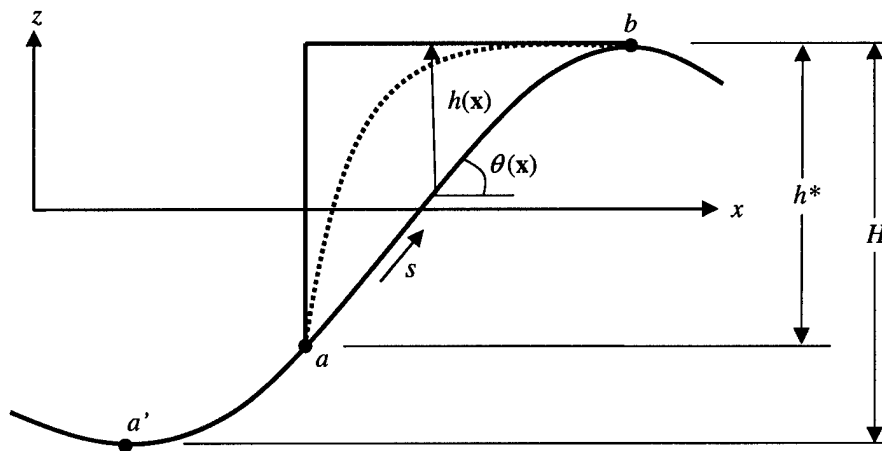


Figure 2. Schematic of the breaker and the definitions of the modeling parameters.

A steady breaker can be modeled using the semi-analytical approach of Cointe & Tulin (1994). In this approach, the breaking region (the region of partially aerated white water forward of the breaking wave crest) is assumed to 'ride' on of the forward face of the wave. At the forward edge of the breaking region, the 'toe' of the breaker, the free-surface streamline becomes submerged under the breaking region and re-emerges at the wave crest (see the blue line in Figure 2). The weight of the breaking region increases the pressure along the free-surface streamline. If one assumes a shape and density for the breaking region, and further that the total head is conserved along the streamline, the velocity and pressure along the free-surface streamline under the breaking region can be determined. These quantities are then used in place of the usual free surface kinematic and dynamic boundary conditions, (3) and (4), respectively. From a momentum conservation standpoint, the force associated with the increased pressure acting on the free-surface streamline results in an increased drag on the hydrofoil, due solely to wave breaking. The approach as implemented can be described in reference to the schematic of the breaking wave crest, shown in Figure 2. Following the Rhee & Stern (2000) implementation, the breaking model is invoked for any wave crests which exhibit $\theta(x) > 15^\circ$ anywhere between the trough and crest. Here, the blue line represents the free-surface streamline s . The dotted line in Figure 2 represents the observed geometry of the breaking region which is approximated by a triangle (the red line). The toe of the breaker is located at the point labeled a , and its location can be specified in different ways; here, we will follow

Muscari & Di Mascio (2003) and define the vertical distance between the crest and the toe (points b and a) as

$$h^* = z_b - z_a = 0.64H, \quad (10)$$

where the choice of the coefficient 0.64 by Muscari & Di Mascio was based on the experimental data of Duncan (1983). It is assumed that there is a discontinuity in the velocity at a , given by

$$u_s(x_a) = \beta u_0(x_a) \quad (11)$$

where β is a 'mixing' parameter with values between 0.5 and 0.7, and the value of $u_0(x_a)$ is determined by applying Bernoulli's equation on the streamline s upstream of a . This yields

$$u_0^2(x_a) = c^2 - 2gz(x_a), \quad (12)$$

where c is the phase velocity of the wave (i.e. the flow velocity far upstream of the foil). In the breaking region, the pressure on the surface between a and b is assumed hydrostatic

$$p(x) = \rho g \left(z(x) + \frac{\rho_{BW}}{\rho} h(x) \right) \quad (13)$$

The ratio ρ_{BW}/ρ represents the ratio between the density of the water/air mixture within the breaker and pure water density. The value for this ratio was estimated by Cointe & Tulin (1994) to be $0.2 \leq \rho_{BW}/\rho \leq 0.6$ where the lower limit represents incipient breaking and the top limit the strong breaking process; a value of 0.5 was used in the calculations. The height of the triangular breaker is calculated as

$$h(x) = z(x_b) - z(x). \quad (14)$$

Streamline velocity for any point between a and b is calculated using the Bernoulli equation and equations (11)–(14):

$$u_s^2(x) = u_s^2(x_a) + 2[p(x_a) - p(x)]. \quad (15)$$

By using the local surface slope, θ , and the streamline velocity u_s , the two surface velocity components are calculated as:

$$u(x) = u_s(x) \cos \theta(x), \quad w(x) = u_s(x) \sin \theta(x) \quad (16)$$

The surface pressure from (13) and the surface-velocity components (15) are then used to specify the boundary conditions in the breaking region.

Short-Wave Modeling

Reynolds-averaged or potential-flow approaches which can be used to calculate the mean surface-elevation and velocity fields; however, the short waves which are responsible for radar backscatter are not resolved using these approaches. The short-wave spectrum is modeled using VSM (Ericson & Wackerman 1999). In that approach, the breaking regions are identified using a vertical acceleration

criterion, an empirical short-wave spectrum is specified in the breaking region, and the evolution of the short-wave spectrum outside the breaking region is calculated using the wave-action balance equations. The breaking criterion is

$$\frac{Dw}{Dt} < 0.15g \quad (17)$$

which identifies regions of large downward acceleration. In these regions the short-wave spectrum is assumed isotropic and is set to

$$S(k) = 0.004\alpha k^{-3.5} \quad k \geq 2\pi/L_b$$

$$= 0 \quad k < 2\pi/L_b \quad (18)$$

where k is the wavenumber and L_b is the length of the breaking region in the wave-propagation direction. The factor α is given by

$$\alpha = \exp\left[-\frac{3.5}{4}\left(\frac{2\pi}{kL_b}\right)^4\right], \quad (19)$$

and is included to yield zero slope in the spectrum at $k = 2\pi/L_b$. It only affects the spectrum very near the cutoff. The propagation of the waves outside the breaking region is done using the wave action-balance equations which govern the evolution of the short-wave spectrum

$$\frac{\partial A}{\partial t} + \nabla \cdot (\mathbf{C}_g A) = \frac{S}{\sigma} \quad (20)$$

where A is the wave-action spectrum (the energy spectral density divided by the wave frequency), \mathbf{C}_g is the vector group velocity (the propagation velocity for the wave energy in both physical and spectral space) and the source term S represents the effects of wind growth, viscous dissipation, etc.

The identification of the breaking region is a key element of the prediction of the short-wave spectrum, as it defines both the location of the breaking regions and the length of the breaking region, L_b . For the radar-cross-section comparisons below, the breaking region was determined in two ways. One was using the native VSM approach (based on the acceleration). The second approach used the information from the breaking model implemented in the RANS code (based on slope).

Radar Backscatter Model

The radar backscatter model used for this study was the small-perturbation method (SPM), described in Ericson et al. (1999). The SPM solution for radar backscatter is given by Valenzuela (1978) as

$$\sigma_{pp}^{SPM} = 8\pi k_0^4 |\gamma_{pp}(\theta_i)|^2 [\Psi(k_b) + \Psi(-k_b)], \quad (21)$$

where Ψ is the surface-elevation energy spectral density, γ_{pp} is a polarization-dependent reflection coefficient, θ_i is the local incidence angle, k_0 is the radar wavenumber, and $k_b = 2k_0 \sin \theta_i$ is the Bragg wavenumber.

RANS Implementation

In this section the implementation issues unique to the hydrofoil-generated waves examined here are discussed. First wave reflections are discussed, along with methods for eliminating them. Then the computational domain is described. Finally the grid requirements are examined.

The results indicate that in order to obtain a RANS solution, the domain must be large and the grid sufficiently stretched eliminate reflection from the upstream and downstream domain boundaries. Additional damping of the waves is sometimes needed. What was also learned is that as long as the flow about the foil is well resolved, the near-field solution for the free surface elevation, and hence the velocity field, will be accurately captured. If the grid resolution away from the foil is not adequate, the far field waves will be attenuated. This near-field accuracy vs. far-field attenuation has been seen in Kelvin-wake predictions, and is tied directly to grid resolution and its impact on wave propagation.

Wave Reflections from Domain Boundaries

The major issue in the simulation proved to be the reflection of waves from both upstream and downstream boundaries. The flow domain is initialized with the flat surface. Waves start to form during the initial transient and the wave train behind the hydrofoil moves towards the downstream boundary. Similarly, a single wave is generated continuously in front of the foil and propagates towards the upstream boundary. Once the waves reach the boundaries, they reflect and cause considerable oscillations in wave amplitudes within the domain. These oscillations are further enhanced at the boundaries and cause severe mass loss. Despite the fact that the calculations can continue in this mode, the convergence rate is reduced and the results lose physical meaning.

Several authors observed the same issue in simulating the free surface flows (Iafrati et al., 2001; Brummelen et al., 2001; Muscari & Di Mascio, 2003). They proposed mesh extensions away from the region of interest thus resulting in increased numerical dissipation. In addition, both Iafrati et al. (2001) and Muscari & Di Mascio (2003) proposed wave damping. We used both methods to prevent the reflected waves. Mesh size was increased geometrically away from the region of interest resulting in cells a few hydrofoil lengths in size. Wave damping was implemented as well:

$$\frac{\partial \eta}{\partial t} + u \frac{\partial \eta}{\partial x} + v \frac{\partial \eta}{\partial y} = w - d\eta \quad (22)$$

where η is surface elevation and d is the damping factor. The damping factor was set to zero in the region of interest and increased geometrically away from it.

Computational Domain

Figure 3 shows details the computational grid or mesh. The mesh had increasingly larger cells away from the hydrofoil towards both ends of the computational domain, as shown in Figure 3a) and Figure 3c). The most commonly used mesh consisted of four blocks, each with 400x20 nodes in the plane. As can be seen in Figure 3b) the mesh around the hydrofoil was non-uniform with refinement in the boundary layer and at the front and trailing edges of the hydrofoil. Flow was quasi two-dimensional with symmetry boundary conditions imposed in the y -direction. Even though the considered geometry was two-dimensional, both UNCLE and CFDSHIP-IOWA can perform only three-dimensional calculations. As a result, simulations performed with UNCLE require meshes at least 3 cells thick, and CFDSHIP-IOWA at least 5 cells thick.

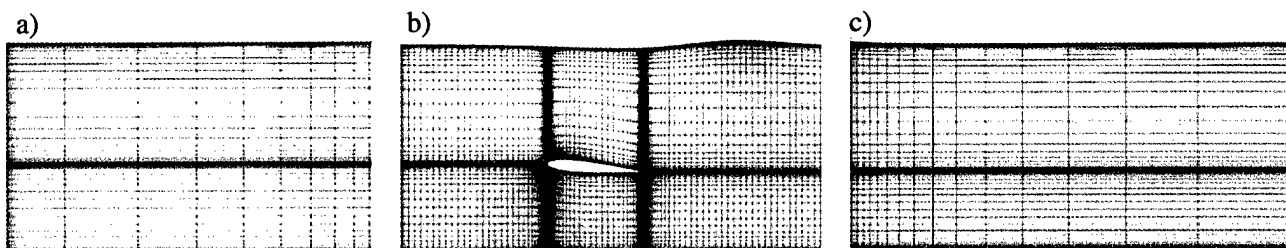


Figure 3. Mesh used in the simulation: a) mesh extension before the hydrofoil, b) mesh detail around the hydrofoil, c) mesh extension after the hydrofoil.

The entire wave profile calculated for the non-breaking wave case measured by Duncan (1983) is shown in Figure 4. The hydrofoil submergence depth in this case was 0.261 m. Observed can be that the surface is flat on both ends of the computational domain. This is a result of using wave damping and large cell sizes that induce large numerical diffusion.

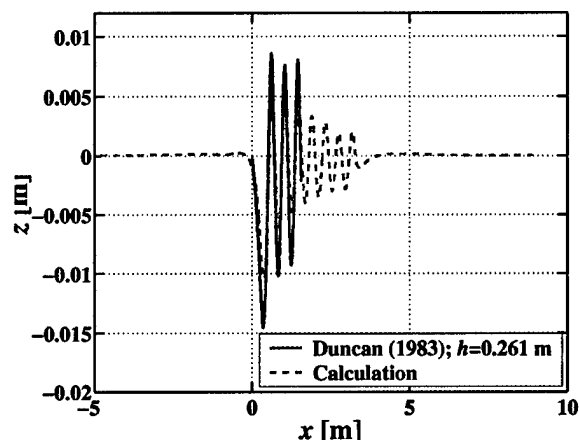


Figure 4. The calculated wave profile for the Duncan 0.261 m case shown for the entire computational domain.

Grid Variations

In order to establish the accuracy of the computations to be presented below for breaking waves, the CFD codes were applied to non-breaking wave cases. In these flows, the grid requirements and overall behavior of the computations were assessed, independent of the complications associated with modeling wave breaking. Simulations of the non-breaking waves were performed using the two RANS codes, CFDSHIP-IOWA and UNCLE. First, the sensitivity of the RANS simulations to the computational mesh was investigated. Next, the description of the RANS calculations and the details of the computational domain and other issues addressed in carrying out the RANS computations are presented.

It should be noted that the grid studies described in this section were carried out using a slightly imperfect geometry for the NACA 0012 hydrofoil used in the experimental work. This has no bearing on the results of the grid study. All the other results were for the precise geometries used in the experiments.

Two mesh types were used in the RANS simulations to verify calculation sensitivity to the mesh type. A number of Cartesian meshes were used to produce most of the results generated for this study. An example of a Cartesian mesh, shown in Figure 5a) had fine grid spacing in the boundary layer, and at the leading and trailing edges of the hydrofoil. This Cartesian mesh had 32,000 points in the x - z plane. In addition to using different grid densities for the Cartesian meshes, a single C-mesh, shown in Figure 5b), was used. In the C-mesh, the grid wraps around the foil and is generally more orthogonal. The C-mesh was refined near the hydrofoil boundary, and it had 85,364 cells in two-dimensions.

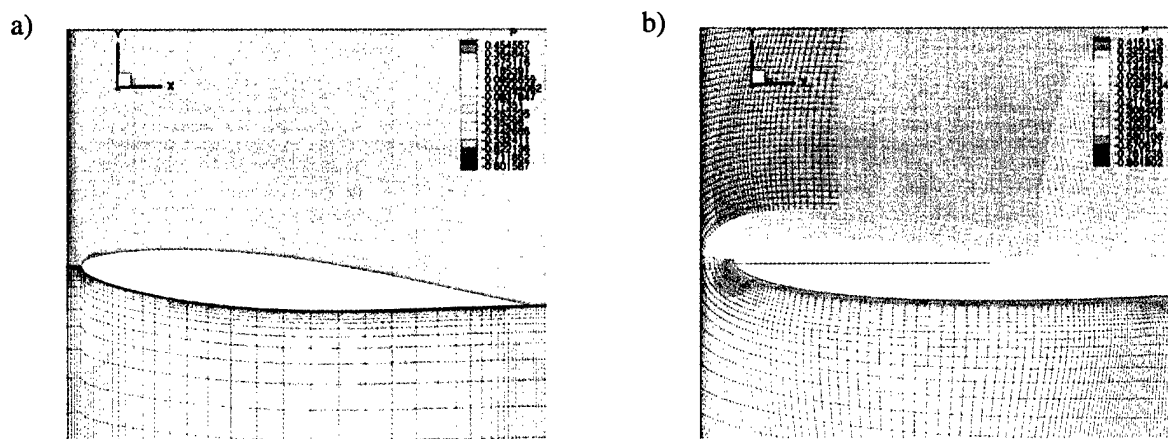


Figure 5. Meshes used in the simulations: a) Cartesian mesh and b) C-mesh.

The comparison between the calculated wave profiles obtained on the two mesh types together with the experimental data are shown in Figure 6a). The predicted location and depth of the trough are in a very good agreement. The result obtained on the C-mesh has a slightly higher crest. This is primarily due to the higher mesh resolution in this case. The predicted pressure coefficient, C_p , distributions along the hydrofoil are shown in Figure 6b) Unfortunately, no experimental data are available for the pressure distribution. Flow acceleration is higher along the top hydrofoil surface in the case with the C-mesh. As a result, pressure drop along the same surface is more than for the Cartesian mesh. Nevertheless, the differences are not large and are not affecting the calculated wave profiles in a significant way. Due to the large number of cases that had to be calculated, increase in the computational time required for the C-mesh could not be afforded and all the simulations were performed on the Cartesian meshes.

The results of a resolution study for the Cartesian meshes are shown in Figure 7. Several calculations were performed with both UNCLE and CFDShip-IOWA codes on meshes ranging from 32,000 grid points in the plane to 121,000 grid points in the plane. The comparison for the wave profiles is shown in Figure 7a). The results are all consistent for the initial trough depth and the height of the first crest. For the coarser meshes, the amplitude of the waves attenuates with downstream distance. The calculated results under-predict the depth of the trough and the height of the measured crest for all cases, when compared to the experimental data. The computational results are almost identical inside the region where the measurement data is available. Similarly, the predicted pressure distributions on the hydrofoil surface shown in Figure 7b) differ only slightly. The behavior of these results are consistent with those

discussed by Reed & Milgram (2000) for RANS calculations of Kelvin wave patterns. They showed that even though RANS computations could accurately reproduce the near-field wave pattern, the waves attenuated rapidly far from the ship. The results shown above indicate that this can be traced to inadequate grid resolution resulting in far-field attenuation.

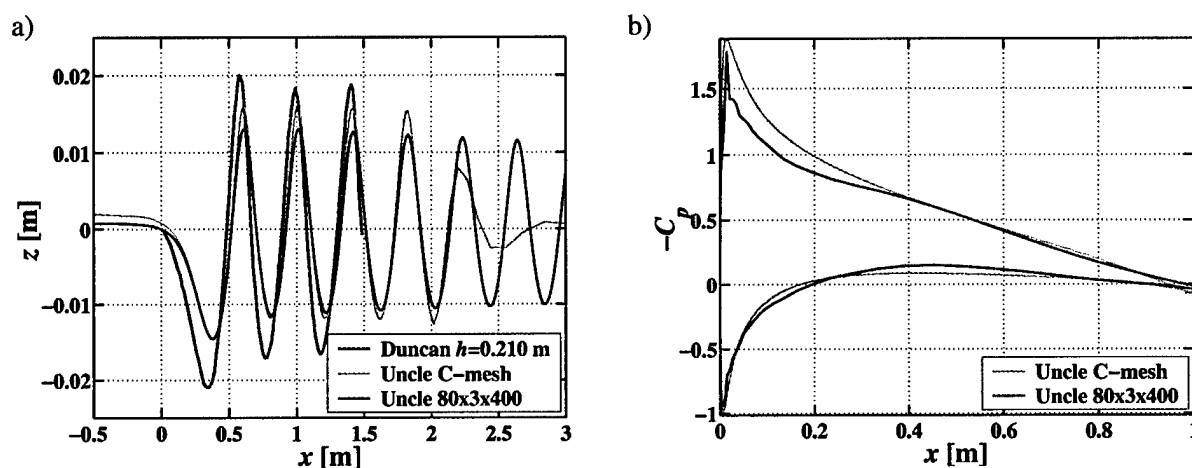


Figure 6. Results calculated on the Cartesian and C-meshes for the Duncan 0.210 m case obtained with UNCLE. Shown are a) wave profiles and b) surface pressure distributions.

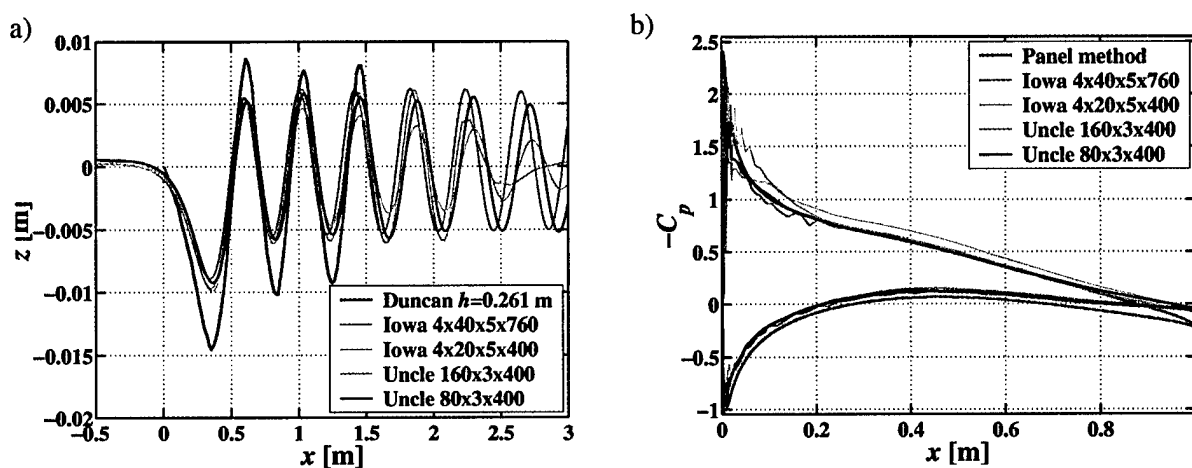


Figure 7. Results calculated with CFDShip-IOWA and UNCLE for the Duncan 0.261 m case. Shown are a) wave profiles and b) surface pressure distributions.

Results

In this section the results from RANS and potential-flow computations for non-breaking are presented. This is followed by results RANS computations for breaking waves using the Cointe & Tulin (1994) breaker model. The section closes with radar cross section computations using the RANS results as input.

For the non-breaking waves, the main results indicate that while RANS and potential flow approaches are capable of accurately calculating the wavelength of hydrofoil-generated stationary breakers, potential flow methods tend to over-estimate the wave amplitude, while RANS appears to under-estimate the amplitude. It should be noted that the amount of data available for comparison is limited in both extent, and type. Velocity fields along with surface elevation profiles would allow more detailed comparisons and more complete validation of calculations.

For the breaking wave cases, three different data sets were examined and the model was shown to have qualitatively correct behavior; i.e. the energy is dissipated and turbulence is produced in the breaking region and the wave amplitude is reduced. The cases of Duncan (1983) were not successfully calculated, either with or without the breaking model. These breakers, including the incipient breaking case could not be converged to a steady solution. Given that steady solutions are obtained for non-breaking wave cases, this points to the breaking model as the problem; however the failure on the incipient breaking case which had a steady non-breaking solution remains unexplained. For the strongly breaking waves of Walker et al. (1996), the trough depth and the wavelength of the waves was well predicted using RANS, but the breaking model is too dissipative and leads to under-estimation of the following-wave amplitude. For the strongest breaker, however, it was not dissipative enough and the breaker height had to be increased to attain a non-overtopping solution. Finally for the cases of Furey et al. (2003), the best match to the data using RANS was obtained with the free-stream velocity set to match the ADV velocity measurements. In general, the wavelength and the initial trough depth were well predicted. The breaking wave crest height was also well predicted at the lower velocities, but over-estimated at the higher velocities, indicating that the level of energy dissipation caused by the model is inappropriate.

Finally, the results of two lower-angle-of-attack cases of Walker et al (1996) were used as input to the VSM radar backscatter model and radar cross-section was estimated for X-Band HH and VV polarization at 45 degrees incidence, looking both up-wave and down-wave. VSM assigns an empirical wave spectrum in the breaking region and calculates the propagation of the short waves outside that region using the wave-action balance equations. The main input to VSM are the surface slopes, surface velocities, and a breaking mask, showing the extent of the breaking region. In addition to RCS, VSM calculates the RMS surface fluctuation level, for comparison to measurements. The RMS surface fluctuations in all cases drop too slowly as the waves propagate downstream from the breaking region. This is traced to the fact that the RANS-predicted velocity in the breaking region is not accurate; this is a limitation of the breaking model which prescribes the surface velocity in the breaking region. Overall the peak RCS values for the breaking region, tend to be over-estimated by up to 5 dB, while the downstream RCS values are over-estimated by up to 25 dB.

Non-Breaking Waves

In order to establish the accuracy of the computations to be presented below for breaking waves, the CFD codes were applied to non-breaking wave cases. Computations were performed using RANS and potential flow. Profiles of non-breaking waves were measured by Duncan (1983) and by Furey *et al.* (2003) and are used for comparison. In general, the results for both approaches match the wavelength of the experimentally observed waves. The potential flow approach, due to its lack of viscous effects will always predict slightly larger lift on the hydrofoil than is realistic and, as a result, it will over-estimate the

initial trough depth and the following wave crest heights. In these results, the potential flow approach predicted initial trough depths and crest height which were generally 10–15% greater than the RANS approach. For the case of Furey et al. (2003), the potential flow approach over-estimated the wave amplitude by about 10%. The RANS computations provide a better match while slightly under-estimating the amplitude; however, there is a positive bias in the RANS results. For the case of Duncan (1983) both approaches under-estimated the wave amplitude by 10% or more. The fact that the measured waves are larger than the potential flow approach predicts may indicate a problem with the data.

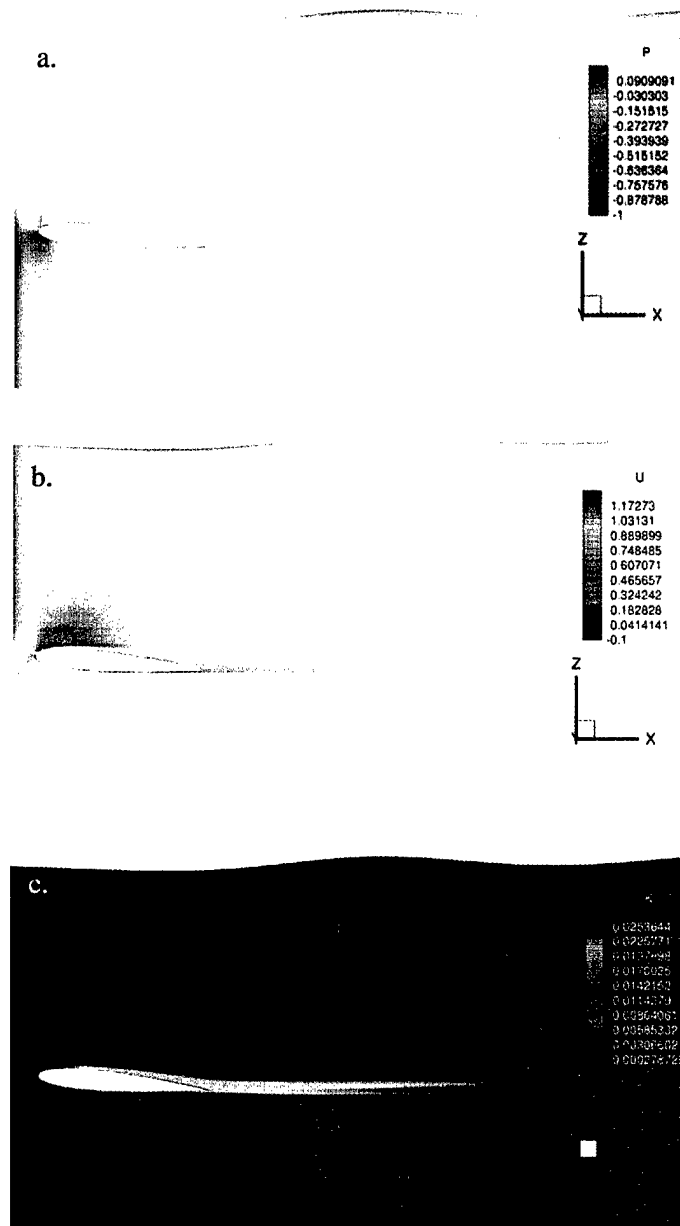


Figure 8. RANS computational results for the flow over the submerged hydrofoil moving with speed 0.8 m/s, depth of submergence 0.261m and angle of attack 5° (Duncan, 1983): a) dynamic pressure field, b) axial velocity field, and c) turbulence kinetic energy field.

The flow field results for Duncan's case are shown in Figure 8. It can be seen that the simulations predict the expected flow behavior. The acceleration of flow above the hydrofoil causes pressure drop and the formation of the first trough. The surface then rises behind the foil for the initial crest. In the velocity field in Figure 8b) and the turbulence kinetic energy field in Figure 8c) the wake of the foil can be seen, but there is no turbulence near the surface since the wave is not breaking. Figure 9 shows a comparison of the measured surface-elevation profile and those computed using the RANS and potential flow approaches. For both approaches, the wavelength of the waves in the computations match the data well. The potential flow results under-estimate the wave amplitude by about 10%, and the RANS results are another 10% lower than that. (The RANS results are for a relatively low resolution computation, and as discussed above, the waves behind initial crest exhibit attenuation; however, the initial trough and crest are unaffected.) Since potential flow results would naturally over-estimate the wave amplitude, and the behavior of the RANS and potential flow results are consistent, there appears to be a problem with this particular data set. This is further supported by the results shown above; this case was used for the grid studies, and was thoroughly examined using multiple grid resolutions, topologies, and even different RANS formulations. All of these were shown to produce consistent results.

Figure 10 shows a comparison of the experimental data of Furey et al. (2003) and results from potential flow and RANS computations. It should be noted that the free stream velocity for the calculations was set to match that measured using the acoustic anemometer downstream of the hydrofoil. For this case, again, the wavelength of the waves is well captured by both approaches. The amplitude of the waves calculated using potential flow is about 10% larger than the experiments indicate; this is consistent with the expectations for potential flow. The RANS results match the amplitude better, within a few percent; however, there is a slight positive bias in the surface elevations estimates.

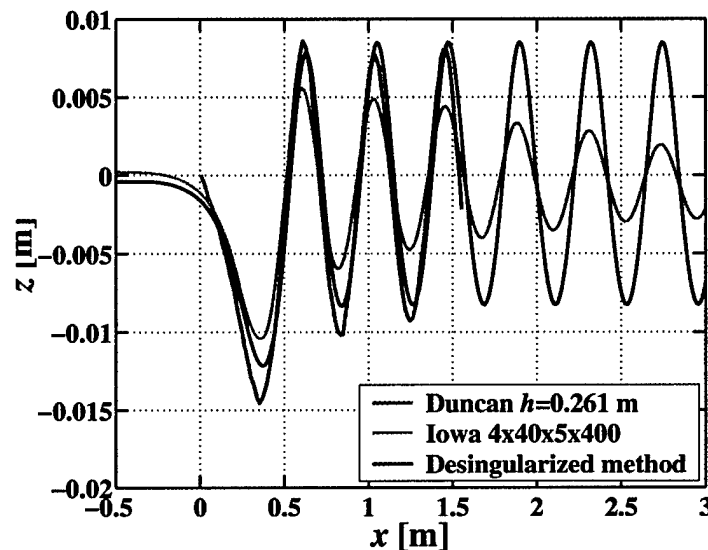


Figure 9. Computational results obtained with CFDSHIP-IOWA and the potential flow code for the Duncan 0.261 m case.

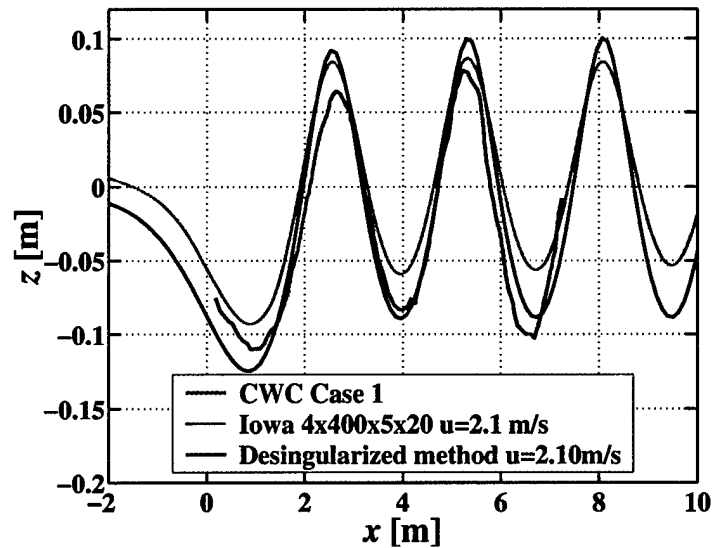


Figure 10. Comparison between the results obtained with CFDShip-IOWA and the potential flow code for the first case by Furey *et al.* (2003) – CWC Case 1.

Breaking Waves

Results for the Cases of Duncan

The measurements by Duncan (1983) were performed using a NACA0012 hydrofoil with a chord of 0.203 m. The upstream velocity was 0.8 m/s, and the hydrofoil angle of attack was kept constant at 5° . The corresponding Reynolds and Froude numbers based on the hydrofoil length were 1.42×10^5 and 0.566. Measurements were performed at varying submergence depths, D . RANS computations were done for $D=0.193$ m, and $D=0.185$ m. The first case was called by Duncan ‘incipient breaking’ because the wave could exist either as a non-breaking wave or a breaking wave depending on whether there were outside disturbances to the free surface. This case was computed with and without the wave breaking model. The final case was a stable breaker, and it was calculated using the breaking model.

Predicted wave profiles together with the measurements are shown in Figure 11. The case at $D=0.193$ m was run for 200,000 time steps and did not achieve a steady solution; i.e. the wave train continued to oscillate in amplitude. After that the simulations were restarted for another 100,000 time steps with the breaking wave model turned on. Experience with other breaking and non-breaking cases indicates that this should have been sufficient to achieve a steady-state solution. Snap-shots of the wave field for both conditions are shown in Figure 11, where it appears that the predicted amplitude and wavelength are reasonable, but the solution would not converge. Also shown in Figure 11 is the result for the $D=0.185$ m case. In this case, similar behavior was observed, with no steady state solution being obtained. Again, the wavelength and amplitude predicted are reasonable.

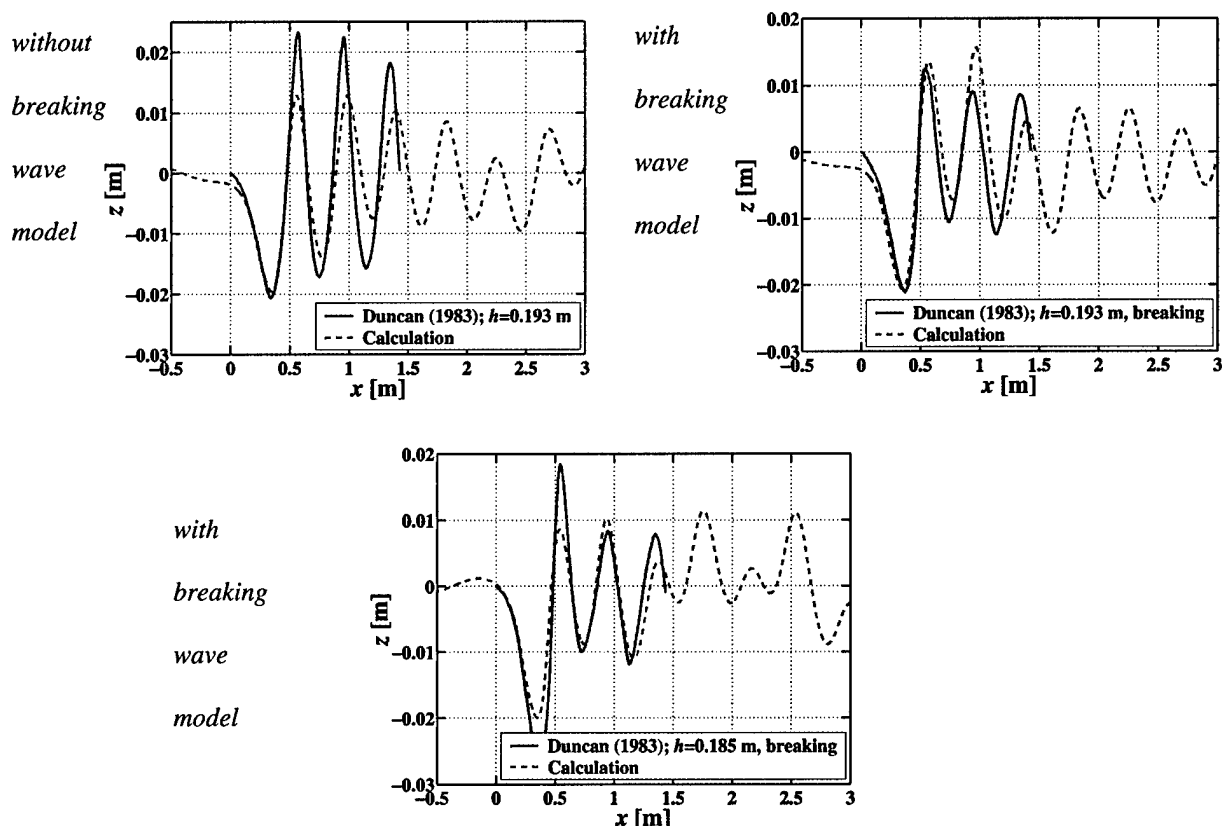


Figure 11. Comparison between the predicted and measured wave profiles for the cases measured by Duncan (1983). Plots on the left and bottom were obtained without the breaking wave model, while plots on the right were obtained with the breaking wave model turned on.

Flow field results are shown in Figure 12. for the the case with the hydrofoil depth equal to 0.185 m. The simulation was done with the wave breaking model. The result of the additional pressure exerted by the breaker on the wave surface can be seen especially in the velocity and turbulence kinetic energy plots. Velocity slows under the breaker, Figure 12b). The velocity discontinuity causes generation of turbulence that can be seen in Figure 12c). In these results, there are no apparent problems which would explain the inability to achieve a steady-state solution. Given that the computational approach works well in the absence of wave breaking, for these breaking or incipient breaking waves, the fault most likely lies with the wave-breaking model.

Results for the Cases of Walker et al.

The measurements done by Walker *et al.* (1996) were performed using the NACA0015 hydrofoil with a 0.304 m chord. The hydrofoil submergence depth was constant at 0.267 m. The upstream velocity varied between 1.08 m/s and 1.10 m/s. The corresponding Reynolds and Froude numbers were 3.30×10^5 and 0.630. The calculations were performed at three different hydrofoil angles: $\alpha=3^\circ$, $\alpha=4^\circ$, and $\alpha=6^\circ$. The Walker *et al.* (1996) measurements were performed at considerably stronger wave breaking conditions (more energy dissipation) than those of Duncan (1983). These cases could not be simulated without the use of the breaking wave model. Without the breaking model the waves tend to overturn almost immediately after the simulation starts. Since the CFD model does not admit overturning waves, the

simulation continues while the results are not physical. Therefore, all the simulations for the Walker *et al.* (1996) cases were done using the breaking wave model.

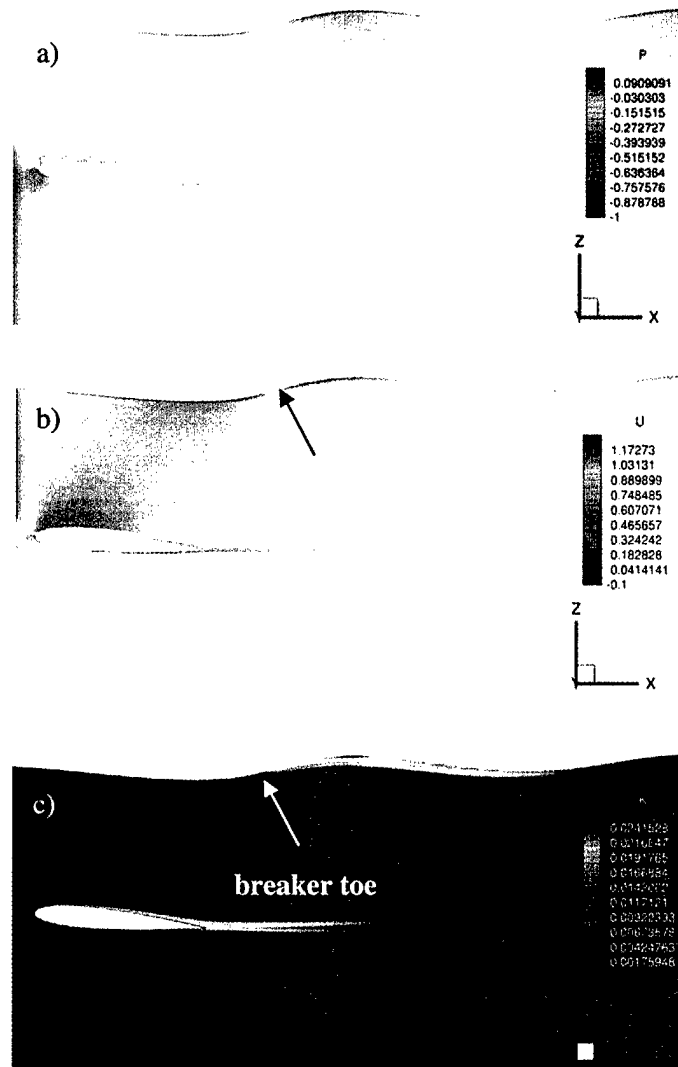


Figure 12. Computational results for the flow over the submerged hydrofoil moving with speed 0.8 m/s, depth of submergence 0.185 m and angle of attack 5° (Duncan, 1983): a) dynamic pressure field, b) axial velocity field, and c) turbulence kinetic energy field.

The results of the RANS calculations for the cases of Walker *et al.* (1996) are shown in Figure 13. Good agreement with the experimental data can be observed for the cases at 3° and 4° hydrofoil angle. The location and depth of the first trough is mostly in agreement with the data, while the following crest is under-predicted. As a result, the following waves are also smaller than measured. The wavelengths and phase of the waves are reasonably well predicted. The good agreement of the initial trough depths indicates the basic RANS solution is reasonable. The under-estimation of the breaking wave crest height is a results of the breaking wave model dissipating too much energy. It should be noted that the breaking

model was mainly developed using the data of Duncan (1983) for waves which were not nearly as dissipative as these.

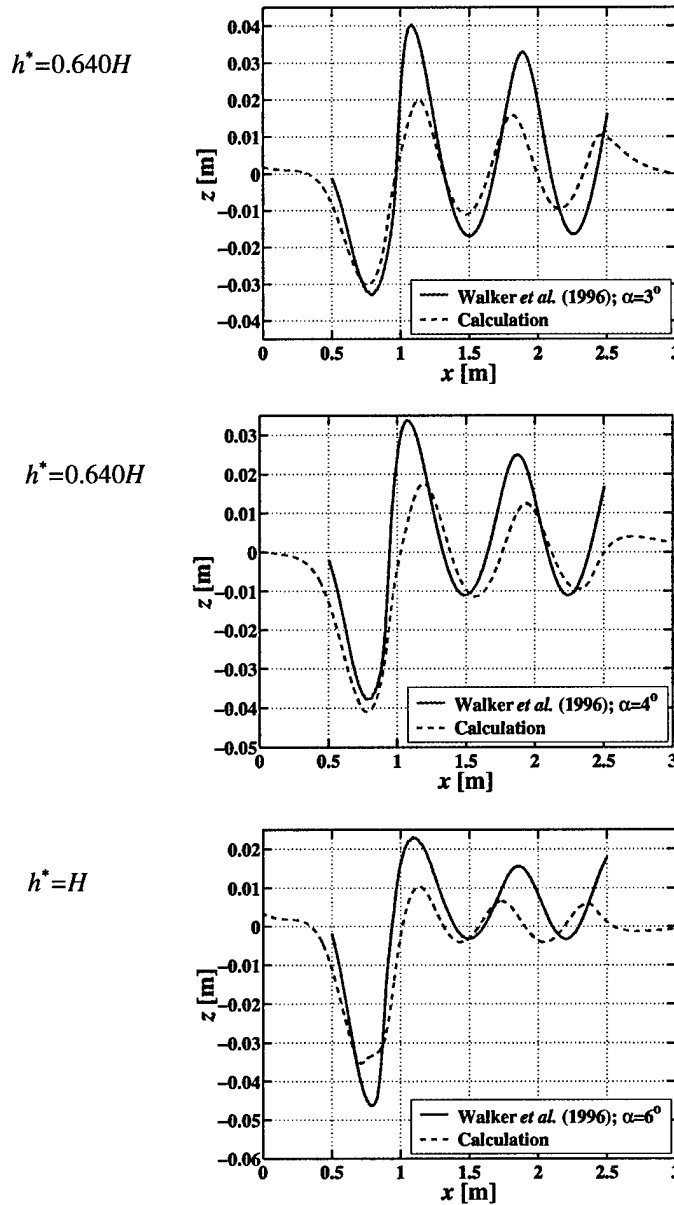


Figure 13. Comparison between the predicted and measured wave profiles for the cases measured by Walker *et al.* (1996). Simulations were performed at different breaker heights, h^* , used in the breaking wave model.

For the 6° case, shown at the bottom of Figure 13, the simulation became unstable and the wave started to overturn, leading to a non-physical solution. The reason for this was that the breaking wave model was not able to dissipate enough energy to stabilize the wave. For this case, the experimentally observed breaker height h^* was approximately equal to the wave height H . Setting $h^* = H$ (rather than the literature

value of $0.64H$) resulted in a stable calculation, but the breaking region was now confined to a small region in the trough of the wave. This results in a strange inflection in the trough of the wave and is probably non-physical.

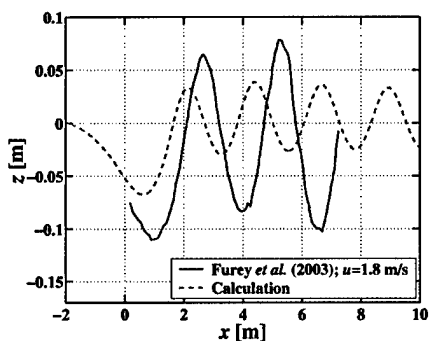
Results for the Cases of Furey et al.

Recently, Furey *et al.* (2003) performed wave measurements in considerably larger channel than the two previous experiments. They used hydrofoil NACA0012 profile with a chord 1.8 m in length. The distance between the channel floor and the hydrofoil attachment point was 0.9 m. Submergence depth varied slightly between 1.75 m and 1.79 m. Hydrofoil angle of attack was set to $5.5 \pm 0.5^\circ$. Measurements were performed at different inlet velocities between 1.8 m/s and 2.6 m/s that were also used in the calculations: $u=1.8$ m/s and $\alpha=5.5^\circ$, $u=2.2$ m/s and $\alpha=5.5^\circ$; $u=2.3$ m/s and $\alpha=5.5^\circ$; $u=2.6$ m/s and $\alpha=5.5^\circ$.

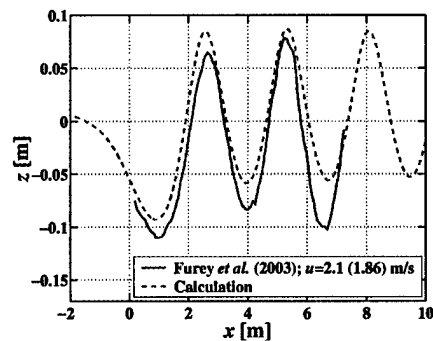
These inlet velocities were measured with a pitot tube upstream of the foil. The simulations were performed using the breaking wave model with the original parameters ($h^*=0.64H$). Comparison between the predictions and the measurements is shown in the left column of Figure 14. The agreement is the worst for the first, non-breaking case. The agreement slightly improves at higher inlet velocities and under breaking wave conditions. However, wave amplitudes are under predicted for all the cases. All calculated troughs are located upstream of their measured location.

Surface velocity was measured also with the acoustic doppler velocimeter (ADV). The ADV- measured velocities were higher than the values obtained using the pitot tube. Another set of calculations was performed with these values at the inlet and the results are shown in the right column of Figure 14. The agreement between the data and the measurements are considerably better. The predicted location of troughs and crests is in agreement with the measurements. The overall wave profiles are in excellent agreement for the first two cases. Further increase in the inlet velocity causes slightly under-predicted troughs and over predicted crests. A possible cause for such behavior might be the deficiency of the wave breaking model.

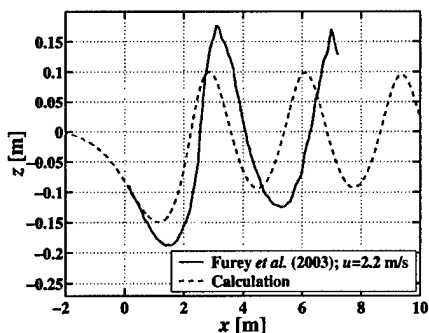
Non-breaking
wave
case



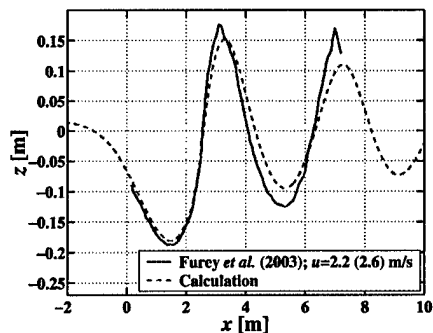
Non-breaking
wave
case



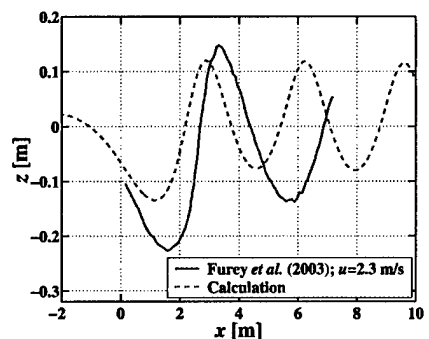
Breaking
wave
case



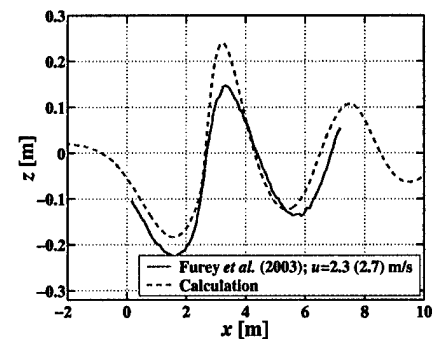
Breaking
wave
case



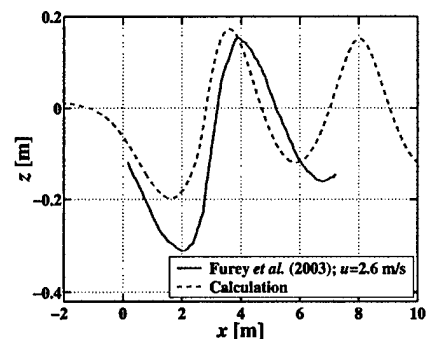
Breaking
wave
case



Breaking
wave
case



Breaking
wave
case



Breaking
wave
case

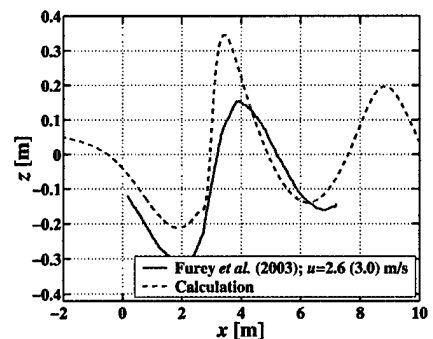


Figure 14. Comparison between the predicted and measured wave profiles for the data by Furey *et al.* (2003). Simulations were performed at inlet velocities measured by the Pitot tube (left column) and by the Acoustic Doppler Velocimetry (right column).

Radar Backscatter Modeling

For the cases of Walker et al. (1996) detailed radar backscatter measurements are available, as presented in that study, and later in Ericson et al. (1999). The modeling approach to be used is the small-perturbation method, or SPM, advanced by Valenzuela (1978). This method was applied to the situation examined here by Ericson et al. (1999), using the experimentally measured short-wave spectrum and surface slope as input to the model. The results are shown in Figure 15, where it is seen that the agreement is quite good for the region downstream of the breaking wave crest. The backscatter from the breaking crest is not well predicted using this model, since the surface roughness exceeds the limits of applicability of the theory. For the up-wave look directions the breaking crest returns are over-predicted for both HH and VV, while for down-wave look direction the breaking crest return is slightly over-predicted for VV and under-predicted for HH. In general, the lack of polarization dependence of the scattering in the breaking region is not captured.

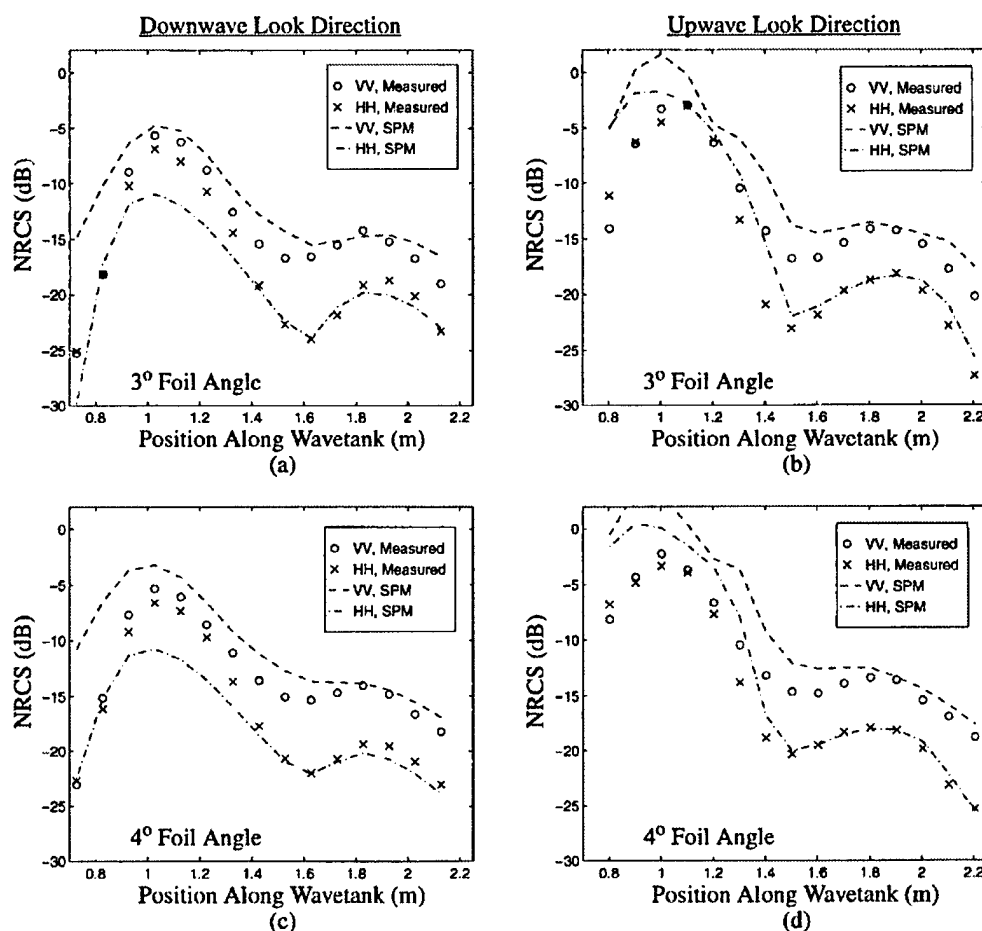


Figure 15. Radar cross-section results for the small-perturbation method (SPM) calculated using the experimentally measured short-wave spectrum, compared to experimental observations for both HH and VV polarization (from Ericson et al. 1999): a) 3 degree angle of attack, down-wave look direction; b) 3 degree angle of attack, up-wave look direction; c) 4 degree angle of attack, down-wave look direction; d) 4 degree angle of attack, up-wave look direction.

It should be noted that in Ericson et al. (1999), the integral equation method (IEM) was the best-performing model over the entire region of interest. For this study, the VSM code was used for the backscatter calculations. The IEM implementation in VSM is only approximate, and not the complete model advanced by Fung et al. (1992) and used by Ericson et al. (1999). For this reason the comparisons presented below are based on the SPM, rather than IEM. Even though the agreement of SPM model is not exact, valid comparisons can still be made. If the hydrodynamic modeling produces a mean surface elevation profile and a short wave spectrum which matches the experimental spectrum observations, the RCS predictions will match those shown in Figure 15.

The hydrodynamic results generated using the RANS models shown above were used as input for VSM. The RCS results from VSM for the 3 degree angle of attack are shown in Figure 16 along with the predicted mean surface elevation and RMS surface fluctuation level. Figure 16 also includes experimental observations for all these quantities.

In Figure 16a) the predicted mean surface elevation is compared to data. As discussed above, the height of the breaking wave crest, and that of the following crests was under-estimated. The model predictions for the RMS surface elevation were obtained by integrating the short-wave spectrum estimated using VSM. Two results are shown in Figure 16b) for comparison to the experimental data: One is that obtained when VSM is allowed to determine the breaking region based on the vertical acceleration. The other is for the breaking region defined by the RANS wave-breaking model. For the former case, the peak RMS surface elevation, which occurs in the breaking crest region, is under-estimated by roughly a factor of two. The modeled RMS decays more slowly than the experiments indicate, and the agreement is not bad downstream of the breaking region. Since the short waves which establish the RMS in this downstream region are generated in the breaking region, and their energy level is too low in the breaking region, the agreement downstream is clearly the result of offsetting errors in the generation and propagation of the short waves. When the RANS code is used to determine the breaking region, the RMS is roughly twice the experimental value in the breaking region, and again decays too slowly downstream. For this case, the RMS remains elevated over the following waves. The reason for the under-estimation for the decay in the RMS surface elevation is discussed below.

Figure 16c)– Figure 16f) show VSM predictions of RCS for the 3 degree angle of attack case for HH and VV polarization and for up-wave and down-wave look direction. Two computational results are shown, one using VSM to determine the breaking region and the other using the RANS-indicated breaking region, along with experimental data from Ericson et al. (1999). First we examine the results for the RANS-indicated breaking. The computational radar backscatter results for the breaking wave crest for HH up-wave (Figure 16c) match the experimental data, while for HH down-wave (Figure 16d) the predictions are roughly 5 dB high. Figure 15a) shows that the ‘correct’ SPM-predicted down-wave HH backscatter from the breaking crest is actually lower by more than 10 dB than for the up-wave look direction. Figure 16c) and d) shows that the RANS-based up-wave and down-wave returns are nearly equal. This discrepancy results from both the error in the size of the breaking region and the lower-amplitude, relatively flat breaking crest. The computational results for VV up-wave in the breaking crest region (Figure 16e) are a few dB higher than the HH results, which is consistent with the data and with the behavior of the SPM model. Similar behavior is seen in the VV down-wave predictions for the breaking crest (Figure 16f). Downstream of the breaking crest, the decay of the radar cross-section mirrors the too-slow decay of the RMS surface roughness, yielding over-estimations of the backscatter by as much as 25 dB, while the modulations have about the right amplitude. For the VSM-indicated breaking, the results are generally similar; however, the lower RMS fluctuation levels results in generally lower backscatter.

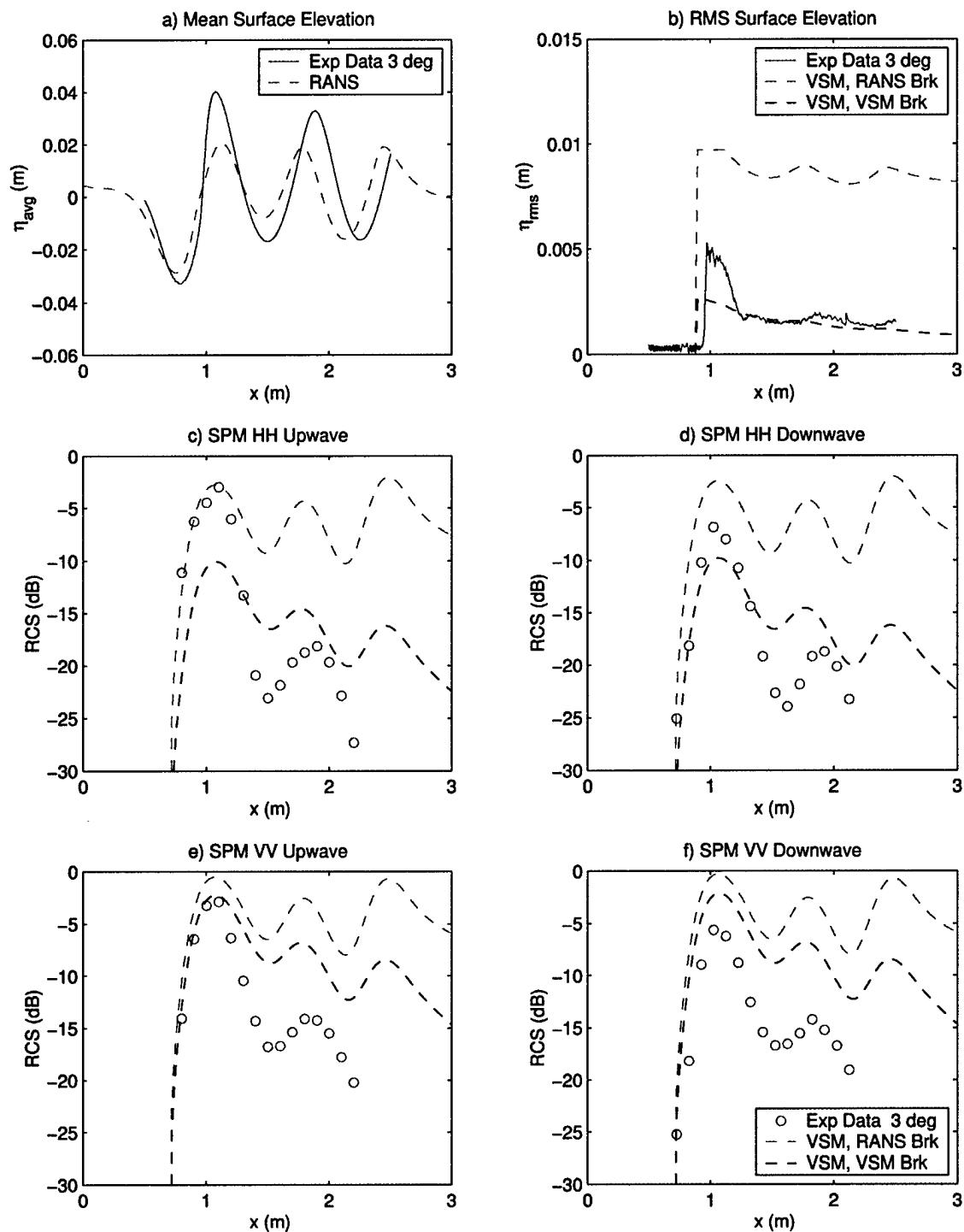


Figure 16. Hydrodynamic and SPM radar backscatter predictions for 3 degree case of Walker et al. (1996): a) mean surface elevation; b) RMS surface elevation; c) radar cross section for HH polarization, up-wave look direction; d) HH, down-wave; e) VV, up-wave; f) VV, down-wave

The lower predicted decay rate of the short waves downstream of the breaking region shown in Figure 16b) is related to the prediction of the velocity field by the RANS models. As the waves generated in the breaking region propagate downstream they interact with an accelerating fluid velocity. This acceleration will reduce the wave energy, i.e. the waves are 'stretched' as they leave the breaking region, lowering their amplitude. The lack of a rapid drop in RMS just downstream of the breaking region indicates that the waves do not undergo this acceleration in the model calculations. This can come about in two possible ways. Since the wave spectrum is prescribed in the indicated breaking region, it is only influenced by the fluid velocities outside this region; hence, if the indicated breaking region extends beyond this area of rapid acceleration, the wave will never experience it. Alternatively if the hydrodynamic model for breaking under-estimates this acceleration, the waves will not be reduced in amplitude as much either. The latter explanation fits the present case; Figure 17 shows a comparison of experimental data for the surface velocity from Ericson et al. (1999) to that obtained using RANS. In the experiments, the velocity in the breaking region is essentially zero; however, the RANS calculations indicate that the velocity in the breaking region is only reduced by half. This indicates that the breaking model is producing a poor estimate of the velocities in the breaking region and this directly affects the short wave spectrum prediction and that for the RMS surface elevation.

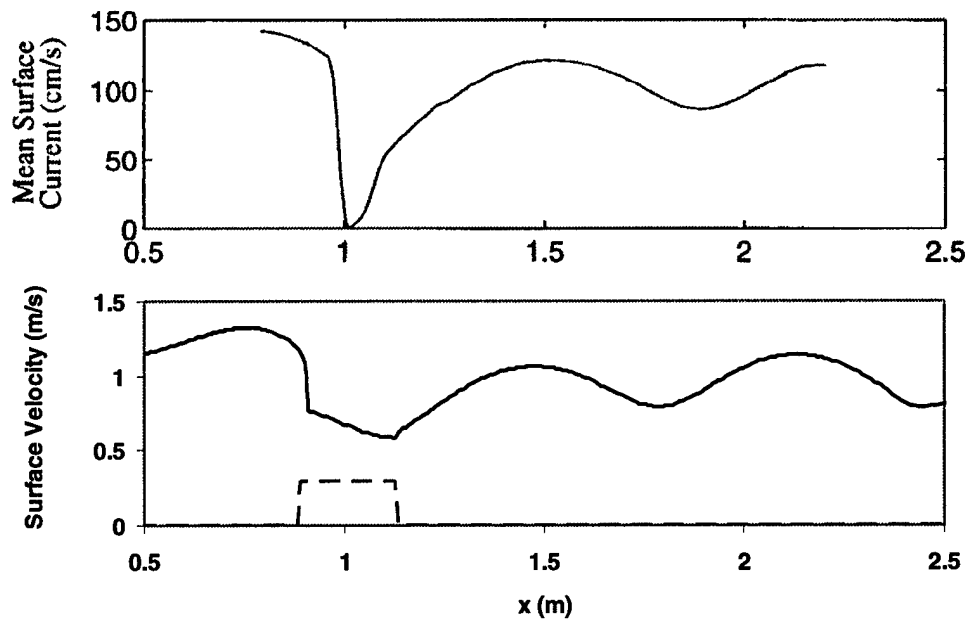


Figure 17. Comparison of measured (upper) and predicted (lower) streamwise velocity components at surface for the 3 degree angle of attack wave from Ericson et al. (1999). Experimental data from Ericson et al., computations using CFDSHIP-IOWA. The dashed red line indicates the location of breaking in the RANS predictions.

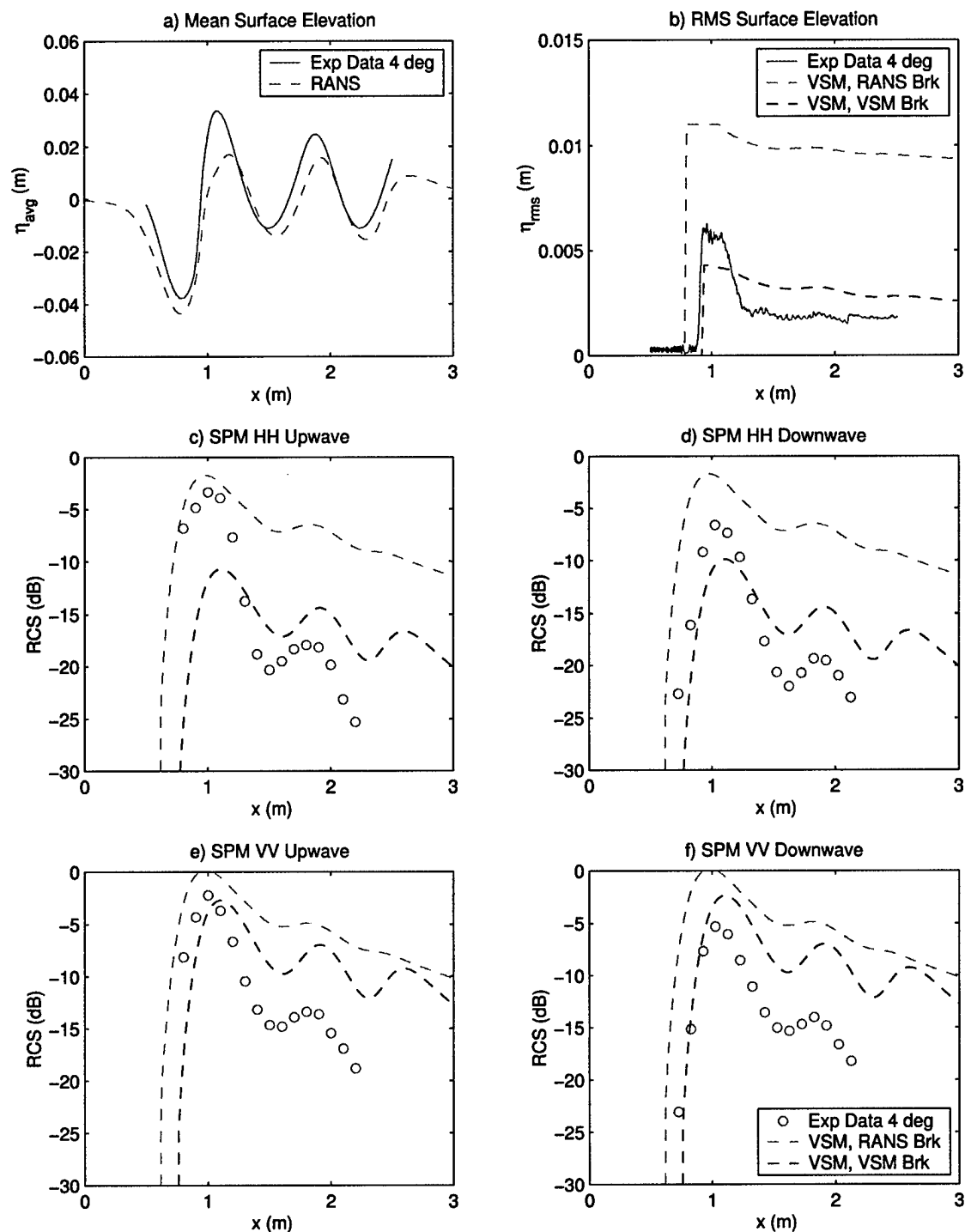


Figure 18. Hydrodynamic and SPM radar backscatter predictions for 4 degree case of Walker et al. (1996): a) mean surface elevation; b) RMS surface elevation; c) radar cross section for HH polarization, up-wave look direction; d) HH, down-wave; e) VV, up-wave; f) VV, down-wave.

Figure 18 shows the results from VSM for the 4 degree case of Walker et al. Overall the behavior is similar to that of the 3 degree case shown in Figure 16. The main difference is the small degree of modulation in the downstream RCS for RANS-predicted breaking region. This is a result of the lower amplitude of the following waves, when compared to the 3 degree case, consistent with greater energy dissipation due to breaking than in the 3 degree case. The difference between the downstream RCS modulations for the RANS- and VSM-indicated breaking regions is due to the broader spectrum (from the larger breaking region) in the RANS case, and the smaller influence of the orbital velocities on the longer waves.

Conclusions and Recommendations

Conclusions

This study had two goals, the first of which was to examine approaches for calculating the hydrodynamics of breaking waves and to assess the impact of hydrodynamic model errors on the prediction of radar backscatter. To address this, RANS computations of stationary hydrofoil-generated breaking waves were carried out, including the modeling of the breaking region. These results were compared to experimental data. A subset of these hydrodynamic results was used as input to the SPM radar backscatter model in the VSM code and the RCS predictions were compared to those obtained using the same model with experimentally measured hydrodynamic inputs. The second goal of this study was to use the information gained through this effort to define the research needs in this area.

The results show that in order to obtain a RANS solution, the domain must be large and the grid sufficiently stretched to eliminate reflection from the upstream and downstream domain boundaries. Additional damping of the waves is sometimes needed. What was also learned is that as long as the flow near the foil is well resolved, the near-field solution for the free surface elevation and velocity field will be accurately captured; however, if the grid resolution is not adequate, the far field waves will be attenuated. This near-field accuracy vs. far-field attenuation has been seen in Kelvin-wake predictions, and is tied directly to grid resolution and its impact on wave propagation.

For the non-breaking waves, the main results indicate that while RANS and potential flow approaches are capable of accurately calculating the wavelength of hydrofoil-generated stationary breakers, potential flow methods tend to over-estimate the wave amplitude, while RANS appears to under-estimate the amplitude. It should be noted that the amount of data available for comparison is limited in both extent, and type. Velocity fields along with surface elevation profiles would allow more detailed comparisons and more complete validation of calculations.

For the breaking wave cases, the breaker model was shown to have qualitatively correct behavior; i.e. energy is dissipated and turbulence is produced in the breaking region and the wave amplitude is reduced, but was not robust or particularly accurate. There were cases which could not be driven to a converged solution. For the strongly breaking waves of Walker et al. (1996), the trough depth and the wavelength of the waves was well predicted using RANS, but the breaking model was too dissipative and led to under-estimation of the following-wave amplitude. For the strongest breaker, however, it was not dissipative enough and the breaker height had to be increased to attain a non-overturning solution. For the cases of Furey et al. (2003), the wavelength and the initial trough depth were well predicted. The breaking wave crest height was also well predicted at the lower velocities, but over-estimated at the higher velocities, indicating that the level of energy dissipation caused by the model is inappropriate at higher speeds.

Finally, the results of two lower-angle-of-attack cases of Walker et al (1996) were used as input to the VSM radar backscatter model and radar cross-section was estimated for X-Band HH and VV polarization at 45 degrees incidence, looking both up-wave and down-wave. In addition to RCS, VSM calculates the RMS surface fluctuation level, for comparison to measurements. The RMS surface fluctuations in all cases drop too slowly as the short waves propagate downstream from the breaking region. This is traced to the fact that the RANS-predicted velocity in the breaking region is not accurate; this is a limitation of the breaking model which prescribes the surface velocity in the breaking region. Overall the peak RCS values, for the breaking region, tend to be over-estimated by as much as 12 dB, and the downstream RCS values tend to be over-estimated by as much as 25 dB. Hence, hydrodynamic errors incurred in modeling breaking waves can lead to significant errors in radar backscatter estimates.

Research Needs

In order to predict the behavior of breaking waves for flows of practical interest, approaches such as the Reynolds-averaged Navier–Stokes equations must be employed. This type of approach requires that some of the details of the flow must be represented by models which need to accurately reflect the physical mechanisms at play. The results of this study indicate areas where more knowledge and understating are required in order to develop the needed models, and point to a requirement for new, more detailed information on the behavior of breaking waves. There are two ways in which this information can be obtained: The first is through direct numerical simulations (DNS) based on numerical solution of the exact governing equations for the three-dimensional time-evolution of breaking waves. DNS allows the details of the waves to be examined both qualitatively and quantitatively, and can provide access to un-measurable quantities such as the subsurface pressure fluctuations. These detailed data can be used to guide the development of the needed models. The drawback to this approach is that presently it can only be applied to small-scale waves (i.e. waves substantially less than a meter in wavelength) and even then it taxes available computing resources. The second approach is experimental studies of breaking waves, where a more limited set of information can be obtained using available measurement technology, but this can be done at larger scale, approaching the scale of situations of practical interest. Detailed measurement of surface structure, velocity and subsurface turbulence are needed. Through a coordinated, combined approach of DNS and experiments, the information necessary to develop first-principles models for wave breaking and the associated small-scale disturbances important for radar backscatter can be obtained.

Beyond the general need for more detailed information about the behavior of breaking waves, the results of this study indicate some specific areas where improvements must be made. The first is application of computational models to steep waves, where more robust and efficient computational approaches are clearly needed. The second is modeling of the effects of wave breaking, where issues such as modeling the turbulence in the breaking region, and appropriate ways to represent free-surface boundary conditions, etc. in the breaking region need to be addressed. And the third is use of hydrodynamic model results in radar backscatter prediction. These point clearly to research needs in these areas and are presented below.

A final issue is the framework within which modeling of breaking waves should be addressed. Unlike potential-flow methods, Reynolds-averaged approaches do not exclude any of the physical processes which naturally occur in wave breaking; however, potential-flow methods are significantly less demanding computationally. While RANS approaches should be able to predict wave breaking accurately, given appropriate models, it would be desirable to be able to use potential flow methods. This is also discussed below.

Application of CFD to Steep Waves

One of the unexpected developments in this study was the difficulty encountered in carrying out the computations of apparently simple, hydrofoil-generated waves, even for steep, non-breaking cases. One of the main difficulties was due to the lack of appropriate radiation boundary conditions, necessary eliminate wave reflections from the domain boundaries. Present approaches extend the size of the domain and introduce either implicit or explicit damping of the waves, so that the waves never actually reach the boundaries. This leads to unreasonably large computational domains and significantly greater computational-time requirements. The other main issue was the need for robustness in free-surface computations. The free-surface-tracking approaches implemented in the codes used above, where the computational domain is mapped to the instantaneous free surface, implicitly assumes that the surface is a single-valued function of the horizontal coordinates. This eliminates the possibility of overturning in the computations and so if breaking is initiated by overturning, this cannot be captured directly. A

computational approach which admits a multiple-valued free surface description, such as a level-set or more robust surface-tracking approach is needed.

Modeling the Effects of Wave Breaking

If a wave becomes steep enough, a portion of its energy is dissipated via wave breaking. Overturning of the crest and turbulence generation, accompanied by transfer of momentum from the wave orbital motions to the mean drift flow accomplish this dissipation. The breaker model investigated here approaches wave breaking by attempting to add an appropriate amount of pressure to the free surface in the breaking region, in an attempt to stabilize it and keep it from overturning. The rate of work done on the surface by this pressure equals the dissipation due to breaking. This approach ignores the fact that in even in the transient leading to ultimately steady breaking, some overturning occurs, and it requires significant empiricism in specifying that stabilizing pressure. A final, robust model for wave breaking will probably not be of this form. The results of this study raises additional significant issues which will need to be addressed by the ultimate approach. These include 1) determining the onset of wave breaking, 2) modeling the generation of surface disturbances in the breaking region, and 3) modeling the generation of waves in the breaking region and their subsequent propagation.

Modeling approaches for the onset of wave breaking do not appear to replicate observed behavior very well. As a wave becomes steeper, the water particle velocities increase roughly in proportion to its steepness. Eventually, as the steepness increases, the water particles near the crest begin to move at a speed greater than the wave propagation velocity. This leads to overturning and collapse of the wave crest into breaking. In present modeling approaches, the onset of breaking is identified by examining wave steepness (greater than 15 degrees) or downward accelerations (greater than $0.15g$). The problem with these approaches is that the thresholds are generally required to be substantially lower than observed in waves just before breaking occurs naturally. In the final model for wave breaking, the natural evolution of a steep wave to a state of breaking should be captured.

The generation of surface disturbances in the breaking region is important for radar backscatter as well as for hydrodynamics. The effects on radar backscatter are clear. For hydrodynamics, the disturbances are caused by the subsurface turbulent fluctuations, and this process affects the dynamics of the turbulence and thereby the overall evolution and behavior of the flow. The generation of surface disturbances has not been investigated significantly, and it is not clear how modeling of this can be accomplished in a RANS context. Presently these disturbances are treated as waves with a prescribed spectrum, but it is not clear that all the surface fluctuations in the breaking region can be appropriately described this way. This is an area where guidance from DNS computations of breaking waves could be of great use for model development.

The disturbances described above, while important in their own right, also serve as initial conditions for waves which propagate through and beyond the breaking region and over the water surface. These waves contribute significantly to radar backscatter. They also interact with the surrounding velocity field and can steepen and break themselves. These waves are described statistically by the wave action balance equations but, given the strong interactions of the waves with other disturbances in the breaking region and the large velocity gradients involved, it is not clear that this description which assumes slow spatial and temporal changes, is adequate. In addition, there are source terms (turbulent wave generation and dissipation) which are recognized as necessary which are not included in the present formulations and require development. This is again an area where DNS would be instructive and useful.

Hydrodynamic Results for Radar Backscatter Modeling

Modeling radar backscatter presently relies primarily on a statistical description of the small-scale disturbances on the water surface along with information on the mean surface slope. In an ideal world, a three-dimensional time-varying description of the water surface at all scales would be obtainable, and from this a radar backscatter model could make use of whatever statistical description of the surface is most appropriate. Since this detailed description is not obtainable for practical flows, hydrodynamic models which produce the necessary statistical description should be the focus of future research. As our understanding of the behavior of the water surface in the breaking region becomes more clear, it may prove that the wave spectrum alone is an inadequate description. In that case, alternative descriptions would need to be explored and may influence the modeling approaches used for the small-scale disturbances, and possibly even those adopted for radar backscatter modeling.

Computational Framework for Wave Breaking Models

A final issue is the framework within which modeling of breaking waves should be addressed. The exact equations are known, but cannot be solved for large-scale flows and so reduced forms of the equations must be used. A Reynolds averaged approach, while approximate, makes no assumptions about the nature of the flow, and includes turbulence and viscous effects. Potential flow formulations require that the flow be inviscid and irrotational, and exclude turbulence. Since turbulence and viscous effects appear to play significant roles in breaking waves, the RANS approach would appear to be a natural framework in which to treat breaking waves; however, the speed at which potential flow computations can be carried out make this an attractive platform for breaking wave computations. Their usefulness will hinge on development of a physically reasonable approach for modeling wave breaking. While potential flow approaches may ultimately prove to be too empirical or ad-hoc, they warrant investigation.

References

- von Brummelen, E.H., Raven, H.C., Koren, B., "Efficient numerical solution of steady free-surface Navier-Stokes flows,," *J. Comp. Physics*, **174**, pp. 120-137, 2001.
- Cointe, R., Tulin, M.P., "A theory of steady breakers," *J. Fluid Mechanics*, **276**, pp. 1-20, 1994.
- Duncan, J.H., "The breaking and non-breaking wave resistance of a two-dimensional hydrofoil," *J. Fluid Mechanics*, **126**, pp. 507-520, 1983.
- Ericson, E.A., Wackerman, C.C. *The theory and implementation of ESM*, ERIM International, Inc. Report No. 1001125-1-T, 2000.
- Ericson, E.A., Lyzenga, D.R., Walker, D.T. "Radar Backscatter from Stationary Breaking Waves," *J. Geophys. Res.*, **104**, pp. 29,679-29,695, 1999.
- Fung, A. K., Z. Li, and K. S. Chen, Backscattering from a randomly rough dielectric surface, *IEEE Trans. Geosci. Remote Sens.*, **30**, 356-369, 1992.
- Furey, D.A., Fu, T.C., Karion, A., Sur, T.W., Rice, J.R., Walker, D.C., "Experimental Study of the Wave Field Produced by Submerged Hydrofoil," 8th Int. Conf. on Numerical Ship Hydrodynamics, Busan, Korea, September, 2003.
- Iafrati, A., Di Mascio, A., Campana, E.F., "A level set technique applied to unsteady free surface flows," *Int. J. Num.l Methods Fluids*, **35**, pp. 281-297, 2001.
- Komen, G.J., Cavaleri, L., Donelan, M., Hasselmann, K., Hasselmann, S., Janssen, P.A.E.M., *Dynamics and Modelling of Ocean Waves*, Cambridge, 1994.
- Kuethe, A. M., Chow, C., *Foundations of Aerodynamics: Bases of Aerodynamic Design*, 4th ed. John Wiley & Sons, Inc., 1986.
- Muscari, R., Di Mascio, A., "A model for the simulation of steady spilling breaking waves," *J. Ship Research*, **47**, pp. 13-23, 2003.
- Paterson, E.G., Wilson, R.V., Stern, F., "General-Purpose parallel Unsteady RANS Ship Hydrodynamics Code: CFDSHIP-IOWA," IIHR Report No. 432, The University of Iowa, November 2003.
- Rhee, S.H., Stern, F., "RANS Model for Spilling Breaking Waves," *J. Fluids Engineering*, **124**, pp. 424-432, 2002.
- Scullen, D. C., Tuck, E. O., "Nonlinear free-surface flow computations for submerged cylinders," *Journal of Ship Research* **39**, 185-193, 1995.
- Scullen, D. C., "Accurate computation of steady nonlinear free-surface flows," Ph.D. Thesis, The Department of Applied Mathematics, The University of Adelaide, 1998.
- Valenzuela, G.R., "Theories for the interaction of electromagnetic and oceanic waves: A review," *Boundary Layer Meteorol.* **13**, 61-85, 1978.

Walker, D.T., Lyzenga, D.R., Ericson, E.A., Lund, D.E., "Radar Backscatter and Surface Roughness Measurements for Stationary Breaking Waves," *Proc. R. Soc. Lond.*, **452**, pp. 1953-1984, 1996.

Appendix: Nonlinear Free-Surface Potential-Flow Computation Involving a Hydrofoil

Methodology

The two-dimensional potential flow and nonlinear free-surface that results from submerging a hydrofoil some fixed depth beneath the free surface of a finite depth of water was computed. The developed computational method is a combination of two potential-flow approaches. An iterative de-singularized approach [1, 2] is used to compute the nonlinear free-surface, and a linearly-varying vortex-strength panel approach, similar to common vortex-panel methods [3, 4], is used to compute the flow about the hydrofoil. Combining these two approaches was achieved through three steps.

First, the de-singularized nonlinear free-surface potential-flow approach, presented by Scullen [1, 2], was implemented and verified. This approach utilizes a distribution of discrete singularities (i.e. sources, doublets, and vortices), placed outside the fluid domain, and an iterative approach to simultaneously satisfy the various boundary conditions at the free surface. At each iteration, new singularity strengths are determined by the solution of a system of linear equations, and the free-surface elevation is updated based on the new pressure distribution at the free surface.

The following set of equations describes the flow that is considered:

$$\nabla^2 \phi = 0 \quad \text{in the fluid domain,} \quad (1)$$

$$E \equiv \frac{Dp}{Dt} = 0 \quad \text{and} \quad (2)$$

$$p = 0 \quad \text{on the free surface,} \quad (3)$$

$$\nabla \phi \rightarrow U_\infty \quad \text{upstream, and} \quad (4)$$

$$\nabla \phi \cdot n = 0 \quad \text{on the body.} \quad (5)$$

Here, ϕ represents the velocity potential, p is the pressure in excess of atmospheric, U_∞ is the upstream speed of the fluid, and n is the unit-normal vector pointing out of the body. Since the pressure is analytically determined, via Bernoulli's equation, as a function of the fluid depth and velocity potential and ϕ identically satisfies Equation 1, the remaining task is to compute the velocity potential and free-surface elevation, η , that simultaneously satisfy the boundary conditions.

Finding this simultaneous solution is a difficult task. However, a systematic solution approach is to iterate between computing the flow beneath an approximate free surface, and using the flow solution to determine a better approximation to the free surface. Iteration continues until the free surface for which the boundary conditions are sufficiently satisfied is determined.

Now the velocity potential and free-surface elevation are decomposed into two parts: a current approximation (denoted with a superscript 0), and a refinement to this approximation (denoted with a superscript 1). Specifically, the respective expressions are $\phi \rightarrow \phi^0 + \phi^1$ and $\eta \rightarrow \eta^0 + \eta^1$. Furthermore,

the *kinematic* (Equation 2) and *dynamic* (Equation 3) boundary conditions are combined into a single free-surface boundary condition

$$E^0 p_z^1 - E_z^0 p^1 + E^1 p_z^0 - E_z^1 p^0 = E_z^0 p^0 - E^0 p_z^0. \quad (6)$$

The use of Equation 6 results in quadratic convergence; however, up to third-order derivatives of the velocity-potential function are necessary. In addition to Equation 6, a “radiation condition” is imposed at two upstream points to keep waves from “radiating” upstream and to ensure that Equation 4 is satisfied. The particular radiation condition suggested by Scullen [1] is

$$x\phi_{xz} + 3\phi_z = 0, \quad (7)$$

which states that the vertical component of the velocity decays in proportion to the inverse cube of distance. By performing the necessary derivatives and expressing the results in terms of ϕ^0 and ϕ^1 (see Appendix A), a system of linear equations can be constructed whose solution determines the refinement to the velocity potential. With this new potential, the refinement to the free-surface elevation is obtained by

$$\eta^1 = -\frac{p^0}{p_z^0}. \quad (8)$$

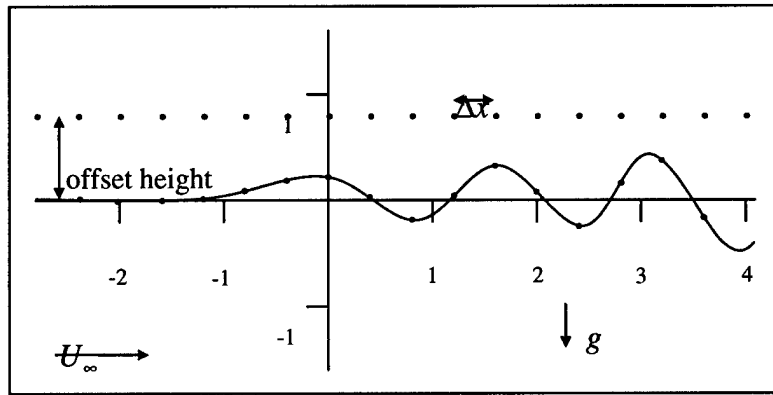


Figure 19: Schematic of free-surface representation.

From an implementation viewpoint, the free surface is discretized with a uniform distribution of collocation points, and discrete sources are placed a fixed distance above each free-surface collocation point. Since Equation 7 is imposed in addition to Equation 6 at two upstream collocation points, two additional sources are used. One is placed upstream to the first collocation point, and the other is placed downstream of the last collocation point while maintaining the same x-axis distribution. This can also be thought of as eliminating the first and last collocation point that would be directly beneath these two sources. The number of sources and their placement are determined based on the work and conclusions of Scullen [1, 2]. While the free-surface collocation points are moved vertically according to Equation 8, the free-surface sources remain fixed. Figure 19 shows a diagram of the free-surface representation.

Scullen also presented results for a submerged cylinder with prescribed circulation. These simulations were performed by specifying body collocation points, and placing sources 85% of the distance along the radius to these collocation points. The circulation was achieved by using a vortex placed at the center of the cylinder and its image above the free surface. While the reason for using the vortex image is not explicitly stated, it is believed that using the image uniquely sets the upstream flow conditions by forcing the far upstream free-surface elevation to be zero. These simulations were reproduced, and the configuration and results for one set of the computations are respectively given in Figure 20 and Figure 21.

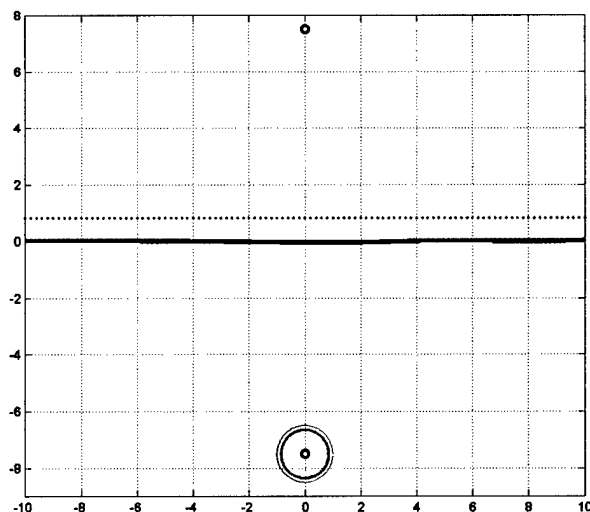


Figure 20: Configuration for radius-to-depth ratio of 0.1333 and a Froude number of 0.3651.

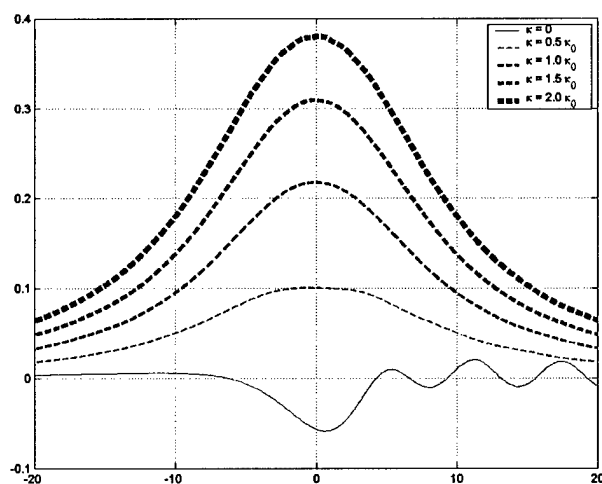


Figure 21: Nonlinear waves produced by cylinders with the above configuration and varying circulation.

Second, the well-established linearly-varying vortex-panel method [3, 4] to compute the flow about a hydro/airfoil was implemented in a way that is compatible with the nonlinear free-surface solution approach described above. The vortex-panel method uses panels to represent the surface of an airfoil, and the distribution of vortex strength along each panel varies linearly from one unknown value at one end to another unknown value at the other end. As a result, integration along the panel is required to compute each panel's contribution to the global potential function (or its derivatives) at any given point in space, i.e.

$$\phi_{panel} = \frac{1}{2\pi} \int_{panel} \gamma(s) \theta(x, z, s) ds. \quad (9)$$

Here, $\gamma(s)$ represents the vortex-strength distribution along the panel and $\theta(x, z, s)$ represents the angle between the line connecting the element ds to the point (x, z) and the x-axis.

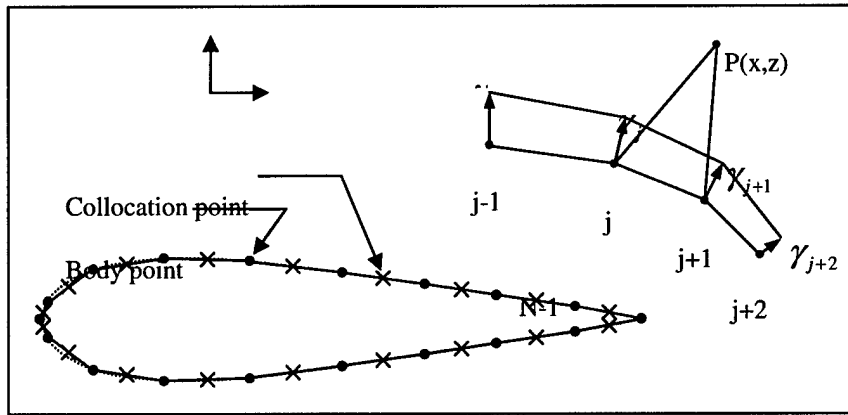


Figure 22: Schematic of the linearly-varying vortex-panel method.

Each panel end point is defined as a point on the surface of the body, and the collocation points are taken to be the panel midpoints. As an implementation note, the N panels are ordered in a clockwise manner, and the surface points are obtained from an analytical correlation to the appropriate NACA 4-digit wing-section data. These and the above-mentioned concepts are illustrated below in Figure 22.

It is easy to see that the Neumann boundary condition (Equation 5), which is imposed at each collocation point on the airfoil, involves first-order derivatives of the velocity potential and is linear with respect to the velocity potential. However, the integral in Equation 9 makes the derivation of the analytical expressions for these quantities more complicated. Typically the integration is performed in a coordinate system that has been rotated such that the x-axis is aligned to the panel and the first end point of the panel, (x_{p1}, z_{p1}) , is at the origin. This rotated coordinate system will be referred to as the panel coordinate system (PCS). Given the angle, β , between the panel and the x-axis in the global coordinate system (GCS), this is achieved through applying the following transformation to the x- and z-coordinates of the point of interest:

$$x_{PCS} = (x_{GCS} - x_{p1}) \cos(\beta) + (z_{GCS} - z_{p1}) \sin(\beta) \quad \text{and} \quad (10)$$

$$z_{PCS} = -(x_{GCS} - x_{p1}) \sin(\beta) + (z_{GCS} - z_{p1}) \cos(\beta) \quad (11)$$

The potential can then be obtained by simply performing the integration and arranging the result in terms of the unknown end-point vortex strengths. The derivatives of the velocity potential, with respect to the GCS, can also be obtained through using Equations 10 and 11 and applying the chain rule of differentiation. (Note: since s is a “dummy” variable, differentiation of Equation 9 with respect to the PCS can be simply taken inside of the integral and is only applicable to $\theta(x, z, s)$.) Appendix A provides explicit expressions for the first-order derivatives of the vortex-panel velocity potential in terms of the end-point vortex strengths.

Since the boundary condition on the surface of a hydrofoil is linear with respect to the velocity potential, the flow solution is typically obtained by solving a single linear system of equations rather than iterating. To reconcile this difference in approaches, the velocity potential corresponding to a vortex panel was also decomposed into an approximation and a refinement to the approximation. With this in place the remaining task was to implement a Kutta condition to close the system of equations and to provide a means to establish the amount of circulation required to properly compute the flow about a lifting body. Typical Kutta condition implementations force the sum of the trailing-edge vortex strengths to be zero, but this will not take into consideration any other sources of velocity potential that might be present. So, an alternative approach [6] was chosen which requires the flow at a point just behind the trailing edge of the hydrofoil to be tangent to the extended symmetry line of the airfoil.

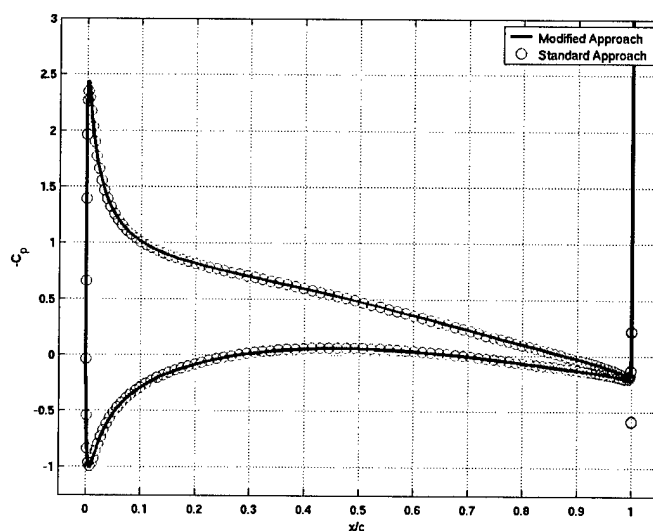


Figure 23: Comparison of flow solutions around a NACA 0012 with an altered and unaltered panel method using 200 panels.

To verify the modified method's implementation, solutions (see Figure 23) for the flow around a NACA 0012 airfoil at an angle of attack of 5° were computed using both an unaltered vortex-panel method code from FDLIB [7] and the described modified method. Both simulations used 200 panels to represent the airfoil. The pressure coefficient distributions shown in Figure 23 are in very good agreement. Both methods display undesirable characteristics near the trailing edge. Wauquier also points this out and describes another type of Kutta condition using a wake panel [4] that improves the solution near the

trailing edge. This Kutta condition implementation, however, was not incorporated into this work. Also note that the analytic correlation that was used for the airfoil does not close at the trailing edge; this could also explain some undesirable behavior near the trailing edge.

Third, the two methods were combined through completing several tasks. Expressing Equation 6 in terms of the velocity potential (See Appendix A.) reveals that up through third-order derivatives are required for the nonlinear free-surface method. Only first-order derivatives are necessary for the panel method. Therefore, the first task was to derive the necessary higher-order derivatives of the velocity potential for a panel. This was accomplished by simply following the same approach that was used to derive the first-order derivatives, and Appendix A provides explicit expressions for the necessary derivatives. Another task necessary to combine the methods was to mirror the vortex panels above the free surface. This is directly analogous to mirroring the single vortex used in the simulations of a cylinder with circulation, except now we are dealing with vortex panels. The last task was to incorporate a method to simulate a finite-depth configuration. This could be achieved by placing sources of unknown strength outside of the domain and below the fluid bottom. The unknown source strengths could then be computed to satisfy the Neumann boundary condition along the fluid bottom. A better approach that does not increase the size of the linear system of equations to solve is to simply mirror every singularity about the fluid bottom. The latter approach implicitly satisfies the Neumann boundary condition along the fluid bottom, and it was utilized in this work.

Results

The method described above was utilized to perform simulations corresponding to configurations used in three sets of experiments. The first set was that of Duncan [5]; the second was performed by Furey, et al [8]; and the third by Walker, et al [9]. Due to limitations of the method to produce solutions for large wave amplitudes, results were obtained for only some of the experiments within the first two sets of experiments. The simulations that produced converged solutions typically involved only non-breaking waves or at most mildly breaking. The simulations that produced converged results are described and presented below.

Duncan [5] performed experiments where a hydrofoil with a NACA 0012 wing section was moved through the water. The hydrofoil with a chord of 0.203 m was given a 5° angle of attack with the pivot point at mid chord. The speed of the hydrofoil was 0.8 m/s, and the hydrofoil was placed 0.175 m above the fluid bottom. In addition to these parameters, experiments were performed with differing free-surface heights above the hydrofoil. The free-surface heights studied include: 0.261 m; 0.236 m; 0.210 m; 0.193 m; and 0.185 m. As the hydrofoil approaches the free surface the resulting wave amplitude increases and wave breaking occurs. Converged solutions were obtained for the first three free-surface heights. For each solution two plots are presented below. The first plot shows the free-surface elevation (with the experimental data, if available), and the second shows the pressure coefficient distribution on the hydrofoil compared with that of a hydrofoil in an infinite domain. Figure 24 through Figure 29 respectively present the results for the first three free-surface elevations above the hydrofoil.

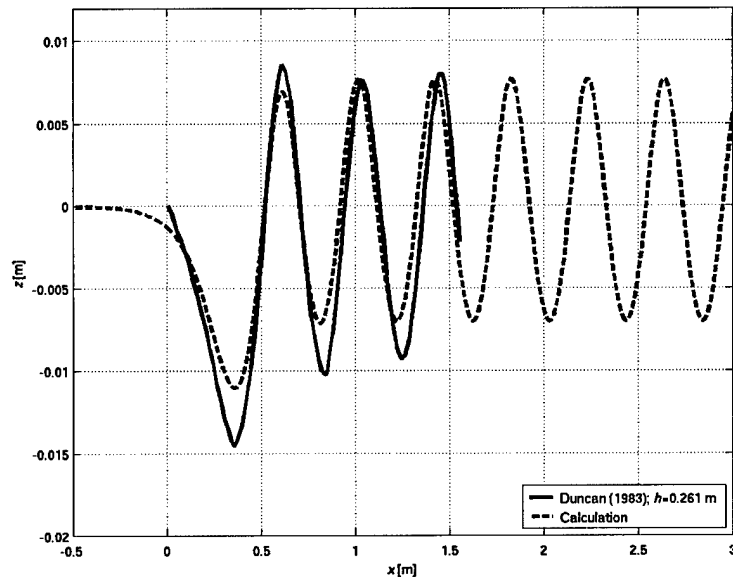


Figure 24: Free-surface elevation for Duncan's depth = 0.261 m case.

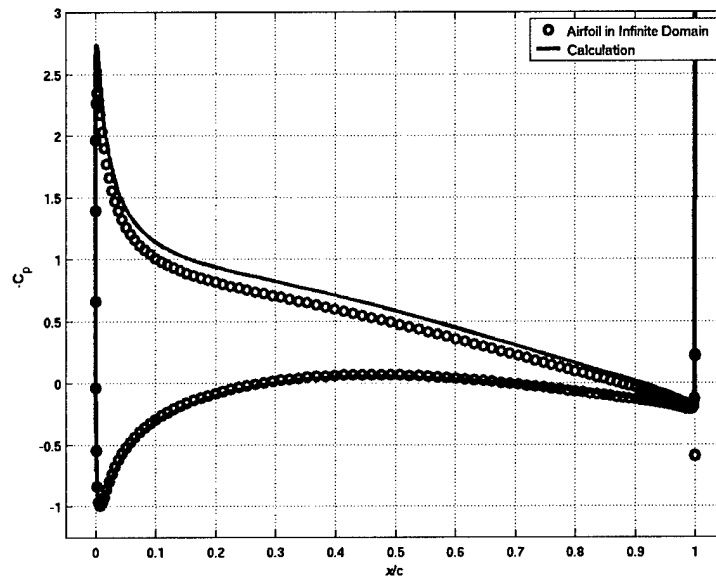


Figure 25: Negative pressure coefficient distribution for the above case.

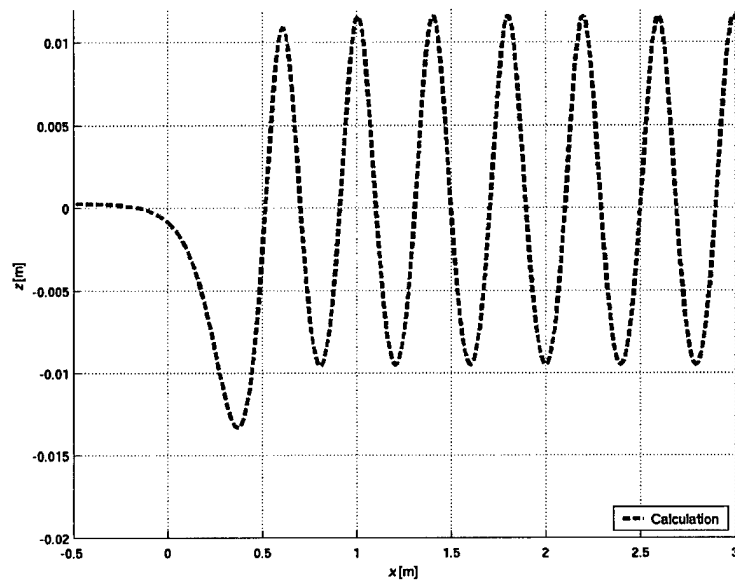


Figure 26: Free-surface elevation for Duncan's depth = 0.236 m case.

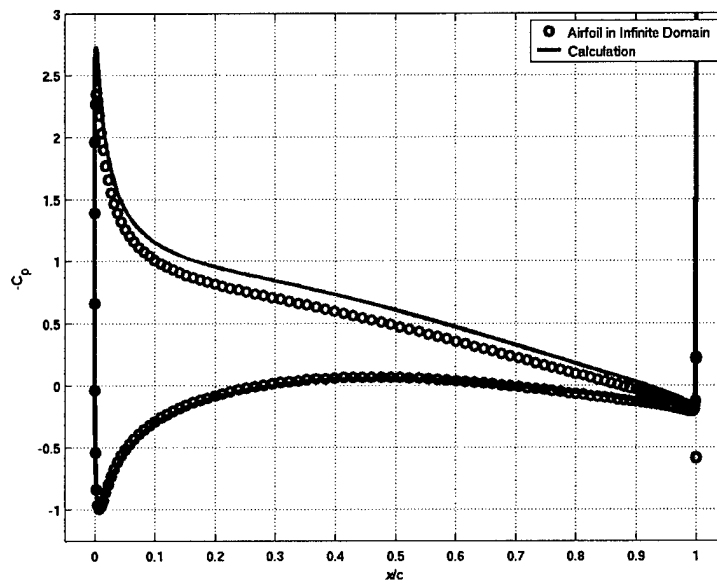


Figure 27: Negative pressure coefficient distribution for the above case.

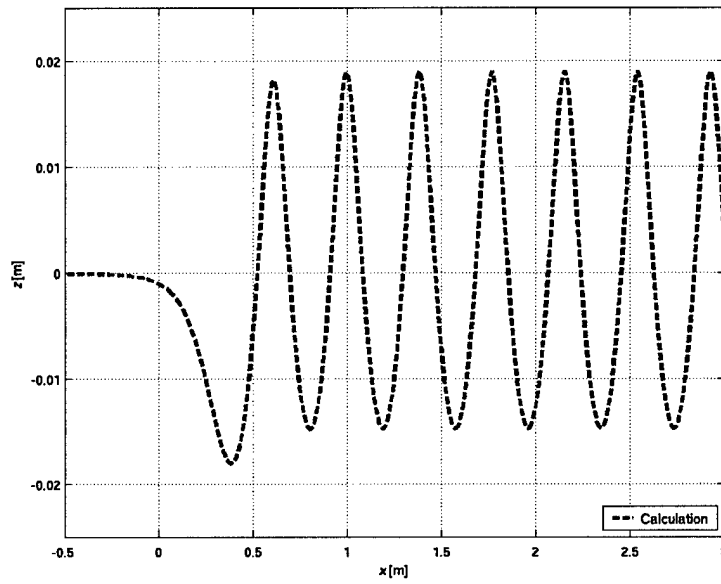


Figure 28: Free-surface elevation for Duncan's depth = 0.210 m case.

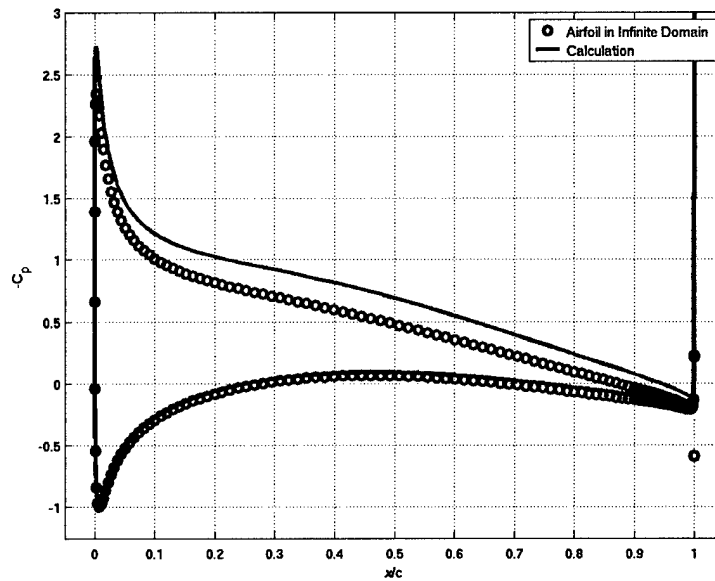


Figure 29: Negative pressure coefficient distribution for the above case.

The four experiments presented by Furey et al [8] also utilize a hydrofoil with a NACA 0012 wing section, but its pivot point is at the quarter-chord position and the flow moves past the hydrofoil. Here the fluid bottom is fixed at 0.9 m below the hydrofoil which has a chord of 1.8 m and an angle of attack equal to 5.5° . Both the undisturbed free-surface elevation and the free-stream velocity are allowed to vary

between experiments. There seems to be some contention regarding whether the reported flow velocities are correct; velocities obtained from an acoustic Doppler velocimeter (ADV) were also available. The ADV velocities were considerably larger. While converged solutions were obtained using both velocities for the first experiment, a solution could be produced for only the lower, non-ADV, velocity for the second experiment. Figure 30 and Figure 31 present results for the first experiment using each free-stream velocity, 1.86 m/s and 2.10 m/s, and an undisturbed free-surface elevation of 1.79 m above the hydrofoil.

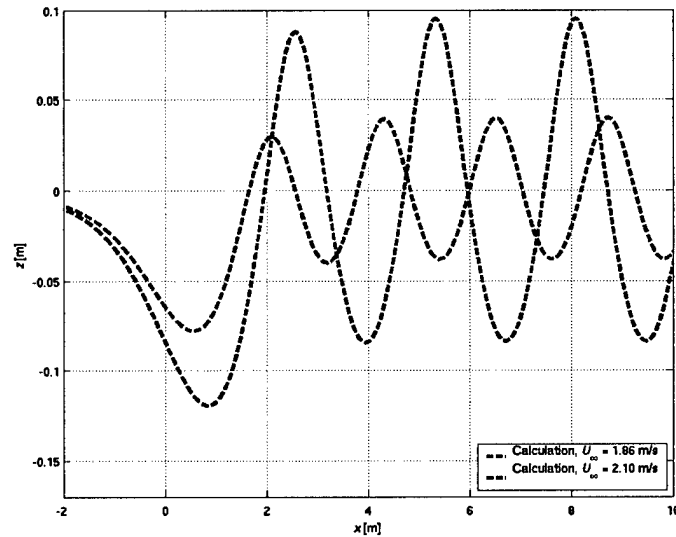


Figure 30: Free-surface elevations for the first case of Furey et al using two different velocities.

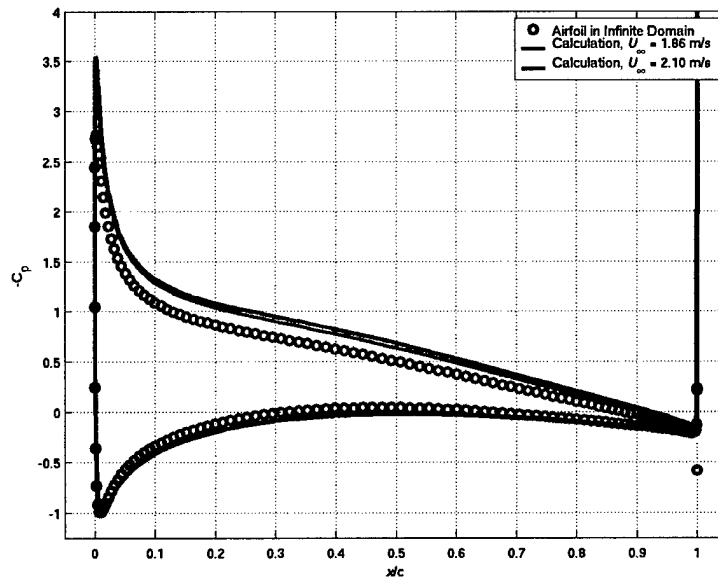


Figure 31: Negative pressure coefficient distribution for the above case.

Nonlinear Free-Surface Expressions

This section presents the components of the free-surface boundary condition in terms of the potentials ϕ^0 and ϕ^1 . It is assumed that the pressure above atmospheric is defined as

$$p \equiv -\frac{p}{\rho} = \frac{1}{2} \left((\phi_x)^2 + (\phi_z)^2 - U_\infty^2 \right) + gz$$

where ρ is the fluid density, g is gravity, and U_∞ is the free-stream velocity. It is also assumed that E is defined as the total derivative of the pressure, i.e.

$$E = (\phi_x)^2 \phi_{xx} + 2\phi_x \phi_z \phi_{xz} + (\phi_z)^2 \phi_{zz} + g\phi_z.$$

With these definitions in place and remembering that $z = \eta^0$ on the free surface, the expressions for the free-surface boundary condition can be derived. While they are presented by Scullen [2], they are presented here as well for completeness. The various components with the corresponding expressions used in this work follow.

$$p^0 = \frac{1}{2} \left((\phi_x^0)^2 + (\phi_z^0)^2 - U_\infty^2 \right) + g\eta^0$$

$$p^1 = \phi_x^0 \phi_x^1 + \phi_z^0 \phi_z^1$$

$$p_z^0 = \phi_x^0 \phi_{xz}^0 + \phi_z^0 \phi_{zz}^0 + g$$

$$p_z^1 = \phi_{xz}^0 \phi_x^1 + \phi_x^0 \phi_{xz}^1 + \phi_{zz}^0 \phi_z^1 + \phi_z^0 \phi_{zz}^1$$

$$E^0 = (\phi_x^0)^2 \phi_{xx}^0 + 2\phi_x^0 \phi_z^0 \phi_{xz}^0 + (\phi_z^0)^2 \phi_{zz}^0 + g\phi_z^0$$

$$E^1 = 2(\phi_x^0 \phi_{xx}^0 + \phi_{xz}^0 \phi_z^0) \phi_x^1 + (\phi_x^0)^2 \phi_{xx}^1 + 2\phi_x^0 \phi_z^0 \phi_{xz}^1 +$$

$$2\left(\phi_x^0 \phi_{xz}^0 + \phi_z^0 \phi_{zz}^0 + \frac{1}{2}g \right) \phi_z^1 + (\phi_z^0)^2 \phi_{zz}^1$$

$$E_z^0 = (\phi_x^0)^2 \phi_{xxz}^0 + 2\phi_x^0 \phi_{xz}^0 \phi_{xx}^0 + 2\phi_x^0 \phi_z^0 \phi_{xzz}^0 + 2\phi_x^0 \phi_{xz}^0 \phi_{zz}^0 +$$

$$2\phi_z^0 (\phi_{xz}^0)^2 + 2\phi_z^0 (\phi_{zz}^0)^2 + (\phi_z^0)^2 \phi_{zzz}^0 + g\phi_{zz}^0$$

$$E_z^1 = 2(\phi_x^0 \phi_{xzz}^0 + \phi_{xz}^0 \phi_z^0) \phi_x^1 + (\phi_x^0)^2 \phi_{xxz}^1 + 4\phi_{xz}^0 \phi_z^0 \phi_{xz}^1 + 2\phi_x^0 \phi_z^0 \phi_{xzz}^1$$

$$2\left((\phi_{xz}^0)^2 + \phi_x^0 \phi_{xzz}^0 + (\phi_{zz}^0)^2 + \phi_z^0 \phi_{zzz}^0\right) \phi_z^1 + (g + 4\phi_z^0 \phi_{zz}^0) \phi_{zz}^1 + (\phi_z^0)^2 \phi_{zzz}^1$$

First-Order Vortex-Panel Velocity-Potential Derivatives

As was stated above, the first-order derivatives of the velocity potential for a vortex panel with linearly-varying vortex strength are obtained by transforming to a coordinate system relative to the panel, denoted PCS, and utilizing the chain rule for differentiation to compute the derivatives in the global coordinate system (GCS). This section provides the results of such a procedure.

Recalling the definition of the transformation from the GCS to the PCS described by Equations 10 and 11, one can obtain the following expressions for the derivative of the PCS with respect to the GCS as

$$\frac{\partial x_{PCS}}{\partial x_{GCS}} = \cos(\beta), \quad \frac{\partial x_{PCS}}{\partial z_{GCS}} = \sin(\beta), \quad \frac{\partial z_{PCS}}{\partial x_{GCS}} = -\sin(\beta), \quad \text{and} \quad \frac{\partial z_{PCS}}{\partial z_{GCS}} = \cos(\beta).$$

Now, the derivative of the velocity potential with respect to x in the GCS becomes

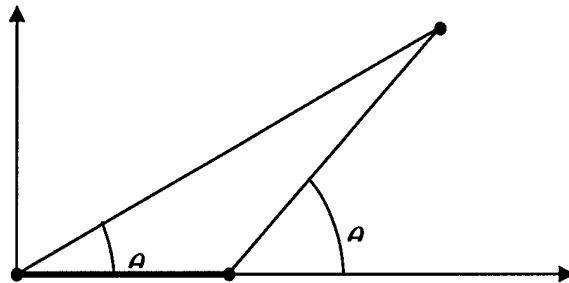
$$\frac{\partial \phi}{\partial x_{GCS}} = \frac{\partial \phi}{\partial x_{PCS}} \frac{\partial x_{PCS}}{\partial x_{GCS}} + \frac{\partial \phi}{\partial z_{PCS}} \frac{\partial z_{PCS}}{\partial x_{GCS}} = \cos(\beta) \frac{\partial \phi}{\partial x_{PCS}} - \sin(\beta) \frac{\partial \phi}{\partial z_{PCS}},$$

and the derivative with respect to z in the GCS is

$$\frac{\partial \phi}{\partial z_{GCS}} = \frac{\partial \phi}{\partial x_{PCS}} \frac{\partial x_{PCS}}{\partial z_{GCS}} + \frac{\partial \phi}{\partial z_{PCS}} \frac{\partial z_{PCS}}{\partial z_{GCS}} = \sin(\beta) \frac{\partial \phi}{\partial x_{PCS}} + \cos(\beta) \frac{\partial \phi}{\partial z_{PCS}}.$$

The remaining task is to express the derivatives of the panel's velocity potential in terms of the end-point vortex strengths, γ_j and γ_{j+1} . In the PCS, the expression for $\theta(x, z, s)$ becomes

$$\theta(x, z, s) = \text{ArcTan}\left(\frac{z_{PCS}}{x_{PCS} - s}\right),$$



$$\begin{aligned}
\frac{\partial \phi}{\partial x_{PCS}} &= \frac{\gamma_j}{2\pi\alpha_2} \left(z_{PCS} \ln \left(\frac{r_2}{r_1} \right) + (x_{PCS} - x_2)(\theta_2 - \theta_1) \right) - \\
&\quad \frac{\gamma_{j+1}}{2\pi\alpha_2} \left(z_{PCS} \ln \left(\frac{r_2}{r_1} \right) + x_{PCS}(\theta_2 - \theta_1) \right), \\
\frac{\partial \phi}{\partial z_{PCS}} &= \frac{\gamma_j}{2\pi\alpha_2} \left((x_{PCS} - x_2) \ln \left(\frac{r_2}{r_1} \right) - z_{PCS}(\theta_2 - \theta_1) + x_2 \right) - \\
&\quad \frac{\gamma_{j+1}}{2\pi\alpha_2} \left(x_{PCS} \ln \left(\frac{r_2}{r_1} \right) - z_{PCS}(\theta_2 - \theta_1) + x_2 \right).
\end{aligned}$$

The following diagram defines the newly introduced terms.

Higher-Order Vortex-Panel Velocity-Potential Derivatives

In a similar fashion the higher-order derivatives of the vortex-panel velocity potential can be derived. Once again, the coordinate transformation definition is used along with repeated use of the chain rule. Further simplifications are also incorporated by using the facts that the velocity potential satisfies the Laplace equation, i.e. $\nabla^2 \phi = 0$, and that the orders of differentiation are interchangeable.

With all of this in mind, expressions for the necessary higher-order derivatives are given below:

$$\begin{aligned}
\frac{\partial^2 \phi}{\partial x_{GCS} \partial x_{GCS}} &= (\cos^2(\beta) - \sin^2(\beta)) \frac{\partial^2 \phi}{\partial x_{PCS} \partial x_{PCS}} - 2\sin(\beta)\cos(\beta) \frac{\partial^2 \phi}{\partial x_{PCS} \partial z_{PCS}}, \\
\frac{\partial^2 \phi}{\partial x_{GCS} \partial z_{GCS}} &= 2\sin(\beta)\cos(\beta) \frac{\partial^2 \phi}{\partial x_{PCS} \partial x_{PCS}} + (\cos^2(\beta) - \sin^2(\beta)) \frac{\partial^2 \phi}{\partial x_{PCS} \partial z_{PCS}}, \\
\frac{\partial^3 \phi}{\partial x_{GCS} \partial x_{GCS} \partial x_{GCS}} &= (\cos^3(\beta) - 3\cos(\beta)\sin^2(\beta)) \frac{\partial^3 \phi}{\partial x_{PCS} \partial x_{PCS} \partial x_{PCS}} + \\
&\quad (3\sin(\beta)\cos^2(\beta) - \sin^3(\beta)) \frac{\partial^3 \phi}{\partial z_{PCS} \partial z_{PCS} \partial z_{PCS}}, \text{ and} \\
\frac{\partial^3 \phi}{\partial z_{GCS} \partial z_{GCS} \partial z_{GCS}} &= (\sin^3(\beta) - 3\sin(\beta)\cos^2(\beta)) \frac{\partial^3 \phi}{\partial x_{PCS} \partial x_{PCS} \partial x_{PCS}} + \\
&\quad (\cos^3(\beta) - 3\cos(\beta)\sin^2(\beta)) \frac{\partial^3 \phi}{\partial z_{PCS} \partial z_{PCS} \partial z_{PCS}}.
\end{aligned}$$

As before, the final task is to compute the panel velocity-potential derivatives. With the same definitions as above, their expressions follow:

$$\frac{\partial^2 \phi}{\partial x_{PCS} \partial x_{PCS}} = \frac{\gamma_j}{2\pi x_2} \left((\theta_2 - \theta_1) - \frac{x_2 z_{PCS}}{r_1^2} \right) - \frac{\gamma_{j+1}}{2\pi x_2} \left((\theta_2 - \theta_1) - \frac{x_2 z_{PCS}}{r_2^2} \right),$$

$$\frac{\partial^2 \phi}{\partial x_{PCS} \partial z_{PCS}} = \frac{\gamma_j}{2\pi x_2} \left(\ln \left(\frac{r_2}{r_1} \right) + \frac{x_2 x_{PCS}}{r_1^2} \right) - \frac{\gamma_{j+1}}{2\pi x_2} \left(\ln \left(\frac{r_2}{r_1} \right) + \frac{x_2 (x_{PCS} - x_2)}{r_2^2} \right),$$

$$\frac{\partial^3 \phi}{\partial x_{PCS} \partial x_{PCS} \partial x_{PCS}} = \frac{\gamma_j}{2\pi} \frac{x_2 z_{PCS}}{r_1^2 r_2^2} \left(\frac{(z_{PCS}^2 - 3x_{PCS}^2 + 2x_2 x_{PCS})}{r_1^2} \right) +$$

$$\frac{\gamma_{j+1}}{2\pi} \frac{x_2 z_{PCS}}{r_1^2 r_2^2} \left(\frac{(z_{PCS}^2 - 3x_{PCS}^2 + 4x_2 x_{PCS} - x_2^2)}{r_2^2} \right), \text{ and}$$

$$\frac{\partial^3 \phi}{\partial z_{PCS} \partial z_{PCS} \partial z_{PCS}} = \frac{\gamma_j}{2\pi} \frac{x_2}{r_1^2 r_2^2} \left(\frac{(3x_{PCS} - x_2) z_{PCS}^2 + (x_2 - x_{PCS}) x_{PCS}^2}{r_1^2} \right) +$$

$$\frac{\gamma_{j+1}}{2\pi} \frac{x_2}{r_1^2 r_2^2} \left(\frac{(3x_{PCS} - 2x_2) z_{PCS}^2 - (x_2 - x_{PCS})^2 x_{PCS}}{r_2^2} \right).$$

References

- [1] D. C. Scullen and E. O. Tuck, *Nonlinear free-surface flow computations for submerged cylinders*, Journal of Ship Research 39 (1995), 185—193.
- [2] D. C. Scullen, *Accurate computation of steady nonlinear free-surface flows*, Ph.D. thesis, The Department of Applied Mathematics, The University of Adelaide, 1998.
- [3] A. M. Kuethe and C. Chow, *Foundations of Aerodynamics: Bases of Aerodynamic Design*, fourth ed. John Wiley & Sons, Inc., 1986.
- [4] C. Wauquiez, *Shape Optimization of Low Speed Airfoils using MATLAB and Automatic Differentiation*, Licentiate thesis, The Department of Numerical Analysis and Computing Science, The Royal Institute of Technology, 2000.
- [5] J. H. Duncan, *The Breaking and Non-Breaking Wave Resistance of a Two-Dimensional Hydrofoil*, Journal of Fluid Mechanics 126 (1983), 507—520.
- [6] C.-Y. Chow, *An Introduction to Computational Fluid Mechanics*, John Wiley & Sons, Inc., 1979
- [7] C. Pozrikidis, *Fluid Dynamics; Theory, Computation, and Numerical Simulation; Accompanied by the Software Library FDLIB*. Kluwer Academic Publishers, 20001.
- [8] D. A. Furey et al, *Experimental Study of the Wave Field Produced by a Submerged Hydrofoil*, 8th Int. Conf. on Numerical Ship Hydrodynamics, September, 2003.
- [9] D. T. Walker, D. R. Lyzenga, E. A. Ericson, and D. E. Lund, *Radar Backscatter and Surface Roughness Measurements for Stationary Breaking Waves*, Proc. R. Soc. Lond 452 (1996), 1953—1984.